s-Nebula: Novel Spin-Based Building Blocks for Advanced TeraHertz Applications

Document Title	Report on ab-initio modelling for spin-based THz emitters		
Document Type Report	Deliverable D3.1	**Authors**	Peter Oppeneer Henri Jaffrès Dominik Legut
Due Date	31/12/2020	**Dissemination Level**	Public
Project	s-Nebula	**Grant number**	863155
Coordinator	THALES SA	**Project Coordinator**	Dr. Romain Lebrun
Call Identifier	H2020-ICT-2019-2020		
Work Package	WP3		
Project Start Date	01/01/2020	**Project Duration**	42 months
Submission Date	30/12/2020		

Report on ab-initio modelling for spin-based THz emitters

Leandro Salemi, Marco Berritta, and Peter M. Oppeneer

Department of Physics and Astronomy,
P. O. Box 516, Uppsala University,
SE-75 20 Uppsala,
Sweden

Henri Jaffrès

Unite Mixté de Physique CNRS/Thales,
University Paris-Sud and Université Paris-Saclay,
91767 Palaiseau,
France

Dominik Legut

IT4Innovations, VŠB-Technical University of Ostrava,
17.listopadu 2172/15,
708 00 Ostrava-Poruba,
Czech Republic

In this deliverable we report on:

(1) *ab initio* calculations that have been performed to obtain accurate values of the decisive materials' quantities in spin-to-charge conversion processes. The responsible quantities are the spin Hall effect (SHE) and the spin Rashba-Edelstein effect (SREE), that convert electric current to spin current and spin accumulation. The inverse of these quantities plays a role in the spin-current driven THz emission. Specifically, we investigate from first-principles the SHE and SREE for thin Pt/$3d$-metal bilayers, such as Pt/Ni and Pt/Co, as well as, for comparison, Pt/Cu and Pt/Pt (without symmetry-breaking at the interface). We furthermore report investigations for the orbital Hall effect (OHE) and the orbital Rashba-Edelstein effect (OREE) that convert charge current in an orbital current and an orbital polarization. The influence of these orbital components on THz emission is as yet unknown. Our atom-resolved calculations determine which of the effects is largest at the interface and how they contribute to the spin-orbit torque (SOT) acting on the magnetization of the $3d$ layer. (UU)

(2) We further study current-induced generation of spin and orbital polarization in the symmetry-broken antiferromagnets (AFM) CuMnAs and Mn_2Au, in the full frequency range. We find that the OREE gives the largest contribution in these materials. (UU)

(3) *Ab initio* calculations have furthermore been performed to compute the spin transparency at the Co/Pt interface. These spin transparencies have been employed to develop a simplified model to predict the THz emission from Co/Pt bilayers that can be compared with the more elaborate superdiffusion model. (CNRS-UMPhy, UU)

(4) Lastly, we report on the electronic properties of bilayer systems that contain layers of Bi or BiSb to study the interfacial Rashba effect and the influence of topological interfaces on spin-charge conversion in Co/BiSb bilayers. (CNRS-UMPhy, VSB)

The work performed under (1), (3) and (4) relates to results obtained in, and investigations currently done in WP1, T1.1. The work performed under (2) relates to tasks T1.3 as well as T2.3. The SOTs calculated under (1) are further relevant for T2.1. The *ab initio* calculations further provide input for the modelling under investigation in T3.2.

CONTENTS

I. *AB INITIO* CALCULATIONS OF CHARGE-SPIN CONVERSION IN PT/3*d*-METAL BILAYERS

A. Introduction and Focus

Ultrafast spin currents, generated by pulsed laser excitation in a ferromagnetic layer, can rapidly penetrate a nonmagnetic layer (Battiato *et al.*, 2012; Eschenlohr *et al.*, 2013; Kampfrath *et al.*, 2013). In the nonmagnetic layer the spin current burst is converted in a transverse charge current through spin-to-charge conversion processes. The resulting short charge current can cause emission of electromagnetic radiation in the THz regime through electric dipole emission (Kampfrath *et al.*, 2013). In the typical case of a bilayer system, consisting of a ferromagnetic (FM) layer and a heavy-metal (HM) layer, the spin-to-charge conversion is believed to occur through the inverse spin Hall effect (SHE) in the heavy-metal layer. The relation between the charge current $\boldsymbol{j}_c$ and the spin current $\boldsymbol{j}_s$ is given by $\boldsymbol{j}_c = \gamma \boldsymbol{j}_s \times \boldsymbol{M}/|\boldsymbol{M}|$, where γ is the inverse spin Hall angle and $\boldsymbol{M}$ the magnetization of the FM layer. The magnitude of the spin Hall angle is given by $\theta_{SH} = |j_s|/|j_c|$, or equivalently, by the ratio of the off-diagonal spin conductivity to the diagonal charge conductivity. A route to optimize the THz emission from the HM layer would thus be to maximize the spin Hall conductivity for a possibly minimized charge conductivity.

The spin-to-charge conversion in a FM/HM bilayer is however a more complex process as the interface can play a role, too, in the conversion. In presence of spacial symmetry-breaking at an interface, a charge current causes a local spin polarization at the interface through the spin Rashba-Edelstein effect (Bychkov and Rashba, 1984; Edelstein, 1990). This effect is different from the SHE which causes spin accumulation due to nonlocal spin transport (D'yakonov and Perel', 1971; Hirsch, 1999). It has been shown recently that this effect can lead to a strong THz emission from Fe/Bi and Fe/Ag/Bi layered structures, where the inverse Rashba-Edelstein effect at the Bi interface is expected to be responsible for the spin-to-charge conversion (Jungfleisch *et al.*, 2018; Zhou *et al.*, 2018). To understand the magnitude and importance of these two spin-charge conversion effects *ab initio* calculations are well-suited. A number of first-principles calculations have been carried out already, primarily focusing on the SHE in metallic layers (Amin *et al.*, 2018; Belashchenko *et al.*, 2019; Freimuth *et al.*, 2014; Mahfouzi *et al.*, 2020; Stamm *et al.*, 2017; Wang *et al.*, 2016). While different *ab initio* calculations for pure Pt do give comparable results (see Stamm *et al.* (2017)) much less is known about the relative size and direction of the SHE and SREE contributions. It is the aim of this investigation to provide values for the SHE and SREE obtained within a unified computational framework.

Both the SHE and SREE are highly relevant as well for the spin-orbit torque (SOT) which has been shown to lead to electrically-induced magnetization switching (Liu *et al.*, 2011, 2012; Miron *et al.*, 2011, 2010). SOT is typically observed in a HM/FM bilayer film where the current flows dominantly through the HM and parallel to the FM layer. In this configuration, reversible magnetization switching can be achieved in a very energy efficient way and, moreover, have read and write currents flow in distinct directions through the device (Baumgartner *et al.*, 2017; Fan *et al.*, 2013; Kim *et al.*, 2013; Safeer *et al.*, 2016). While it is evident from experiments that the SOT can be used to efficiently reverse the magnetization in the magnetic layer, its microscopic origin is still to be fully understood. Within s-Nebula, understanding the SOT is important for spin-based THz detection in WP2.

Similar to the case of pulsed THz emission, two candidates for the SOT have attracted much attention: the SHE (D'yakonov and Perel', 1971; Hirsch, 1999) and the SREE (Edelstein, 1990). Both effects are caused by the spin-orbit interaction, either in the bulk of the material or at an interface, yet their microscopic appearance is drastically different. The nonlocal SHE generates the flow of a transverse spin current to the boundary of the conducting slab (see Hoffmann (2013); Kato *et al.* (2004a); Sinova *et al.* (2015); and Wunderlich *et al.* (2005)) where it exerts a torque on the adjacent ferromagnetic layer. The local SREE (Edelstein, 1990) generates a nonequilibrium spin polarization at a symmetry-broken interface in the presence of Rashba spin-orbit coupling (SOC) (Bychkov and Rashba, 1984). Both effects have been discussed in the context of SOT switching, in some cases the SHE was considered as the dominant effect (Liu *et al.*, 2011, 2012) whereas in other cases the focus was on the SREE (Ciccarelli *et al.*, 2016; Kim *et al.*, 2013; Miron *et al.*, 2011, 2010). In bilayer structures both effects are present simultaneously and will contribute both to the field-like SOT and damping-like SOT (Amin and Stiles, 2016; Belashchenko *et al.*, 2019; Berger *et al.*, 2018; Freimuth *et al.*, 2014; Mahfouzi and Kioussis, 2018; Mahfouzi *et al.*, 2020; Wimmer *et al.*, 2016), yet their relative contribution remains disputed and continues to be a topic of contemporary investigations (Du *et al.*, 2020; Fan *et al.*, 2014; Zhu and Buhrman, 2020) (see also (Manchon *et al.*, 2019) for a recent review).

The SOT can thus be understood as being due to the direct charge-to-spin conversion of the SHE and SREE, whereas the THz emission is based on the inverse process, spin-to-charge conversion. Utilizing first-principles calculations we can thus make a quantitative comparison of the two effects and obtain insight in their detailed microscopic origin.

The SHE and SREE are however not the only magnetic effects that can occur. It was discovered theoretically that, in addition to the spin polarization induced by a current through the SHE, also a nonequilibrium or-

bital polarization can be induced, which represents an orbital Hall effect (OHE) (Go *et al.*, 2018; Go and Lee, 2020; Guo *et al.*, 2005; Kontani *et al.*, 2009; Tanaka *et al.*, 2008). Similarly, the presence of spatial symmetry breaking in a material was recently shown to lead to a local orbital polarization, i.e., an orbital Rashba-Edelstein effect (OREE) (Salemi *et al.*, 2019). Both the OHE and OREE are currently only poorly understood, in terms of their relative magnitudes as well as directions of the induced orbital torques. So far several first-principles calculations have been reported for the OHE (Go *et al.*, 2018; Go and Lee, 2020; Guo *et al.*, 2005; Kontani *et al.*, 2009; Tanaka *et al.*, 2008). A direct observation of the induced orbital polarization is yet to be achieved in experiments (see Refs. Stamm *et al.* (2019) and Xiao *et al.* (2020) for recent studies).

In this Section of the deliverable, we employ relativistic density functional theory (DFT) and Kubo linear-response theory to compute the spin and orbital response to an external electric field for realistic metallic bilayer structures in which Pt is chosen as the heavy-metal material. Specifically, four different systems are investigated: a pure Pt system and three Pt/3d-metal bilayer systems, where the 3d element is Ni, Co or Cu. For these we compute the spin and orbital conductivity and magneto-electric (ME) tensors resolved for the individual atomic layers in the metallic heterostructures, from which we can quantitatively compare the current-induced local and nonlocal spin and orbital polarizations.

In the following, we first introduce the theoretical framework of linear response within DFT and subsequently apply our formalism to compute the spin and orbital responses for the considered bilayer systems, for various Pt thicknesses. We analyze the spatial symmetry of the spin response, which is embodied in the spin ME susceptibility tensor $\boldsymbol{\chi}^s$, and show how it depends on the relative direction of the induced spin polarization $\delta \boldsymbol{S}$ with respect to the applied electric field $\boldsymbol{E}$, the equilibrium magnetization direction $\boldsymbol{M}$, and the system geometry. The tensors can be decomposed into odd-in-$\boldsymbol{M}$ and even-in-$\boldsymbol{M}$ components and thereby provide insight in the distinct microscopic origins (as SHE and SREE) of SOT. The relative importance of those tensor contributions strongly depends on the position of the atomic layer in the slab, and, to a lesser extent, to the thickness of the Pt slab. We investigate furthermore the magnetization-direction dependence of the spin responses and use symmetry relations to keep track of individual components efficiently. We perform a similar analysis for the OHE and OREE. Whereas quantities associated with the SHE, SREE and OREE are spin-orbit induced, a nonzero OHE is present in the absence of spin-orbit interaction. Finally, we discuss the relationship between the components of $\boldsymbol{\chi}^S$ and the SHE/SREE, comparing their relative magnitude. We find that the induced spin polarization at the Pt/Ni and Pt/Co interfaces is mainly

due to the SHE, whereas the SREE-like component plays a bigger role for the top ferromagnetic Ni and Co layers. The orbital polarization is practically completely due to the OHE. We compute effective spin-orbit torques on the magnetic Ni and Co layers and compare our results with previously reported values.

B. Theory

1. Linear response

The materials are modeled within DFT by the relativistic Kohn-Sham Hamiltonian as implemented in WIEN2k (Blaha *et al.*, 2018),

$$\hat{H}_0 |n\boldsymbol{k}\rangle = \epsilon_{n\boldsymbol{k}} |n\boldsymbol{k}\rangle \tag{1}$$

where $\hat{H}_0$ is the relativistic Kohn-Sham Hamiltonian, $|n\boldsymbol{k}\rangle$ the single-electron Kohn-Sham state for band n at wavevector $\boldsymbol{k}$ and $\epsilon_{n\boldsymbol{k}}$ the corresponding eigenenergy. Under the influence of an external perturbation $\hat{V} = -e\hat{\boldsymbol{r}} \cdot \boldsymbol{E}$ where e is the electron charge, $\boldsymbol{E}$ the external electric field and $\hat{\boldsymbol{r}}$ the position operator, the change $\delta \boldsymbol{A}$ in expectation value of a vectorial observable $\mathcal{A}$ associated to vector operator $\hat{\boldsymbol{A}}$, can be expressed within the linear-response formalism (Freimuth *et al.*, 2014; Guo *et al.*, 2008; Mahfouzi and Kioussis, 2018; Wimmer *et al.*, 2016) as

$$\delta A_i = \sum_{j=x,y,z} \chi_{ij}^A \, E_j. \tag{2}$$

The response χ_{ij}^A is expressed in terms of solutions of $\hat{H}_0$,

$$
\chi_{ij}^A = -\frac{ie}{m_e} \int_\Omega \frac{d\boldsymbol{k}}{\Omega} \sum_{n \neq m} \frac{f_{n\boldsymbol{k}} - f_{m\boldsymbol{k}}}{\hbar \omega_{nm\boldsymbol{k}}} \; \frac{A_{mn\boldsymbol{k}}^i \, p_{nm\boldsymbol{k}}^j}{-\omega_{nm\boldsymbol{k}} + i\tau_{\text{inter}}^{-1}} \\
- \frac{ie}{m_e} \int_\Omega \frac{d\boldsymbol{k}}{\Omega} \sum_n \frac{\partial f_{n\boldsymbol{k}}}{\partial \epsilon} \; \frac{A_{nn\boldsymbol{k}}^i \, p_{nn\boldsymbol{k}}^j}{i\tau_{\text{intra}}^{-1}}.
\tag{3}
$$

with m_e the mass of the electron, $f_{n\boldsymbol{k}}$ the occupation of Kohn-Sham state $|n\boldsymbol{k}\rangle$, Ω the Brillouin-zone volume, $p_{nm\boldsymbol{k}}^j$ the $\hat{p}_j$ momentum-operator matrix element, $A_{mn\boldsymbol{k}}^i$ the $\hat{A}_i$-operator matrix element and $\hbar \omega_{nm\boldsymbol{k}} = \epsilon_{n\boldsymbol{k}} - \epsilon_{m\boldsymbol{k}}$, the difference of Kohn-Sham eigenergies. As discussed below, we use for $\hat{\boldsymbol{A}}$ the spin and orbital angular momentum operators, $\hat{\boldsymbol{S}}$ and $\hat{\boldsymbol{L}}$, as well as the the spin and orbital current-density operators, $\hat{\boldsymbol{J}}^{\boldsymbol{S}}$ and $\hat{\boldsymbol{J}}^{\boldsymbol{L}}$. The quantity τ_{inter} (τ_{intra}) is the electronic lifetime for inter (intra) band transitions. In this work, τ_{inter} and τ_{intra} are set to $\hbar \tau_{\text{inter}}^{-1} = 0.272$ eV and $\hbar \tau_{\text{intra}}^{-1} = 0.220$ eV. Those values have been determined by comparing linear-response calculations to experimental conductivity data for Pt thin films (Stamm *et al.*, 2017).

2. Angular momentum and flow of angular momentum

The induced angular momentum is composed of a spin and orbital contribution. Let us first focus on the spin part.

The spin operator $\hat{\boldsymbol{S}}$ and spin-density current operator $\hat{\boldsymbol{J}}^{S_k}$ can be defined as

$$\hat{\boldsymbol{S}} = \frac{\hbar}{2}\left(\hat{\sigma}_x, \hat{\sigma}_y, \hat{\sigma}_z\right), \tag{4}$$

$$\hat{\boldsymbol{J}}^{S_k} = \frac{\{\hat{S}_k, \hat{\boldsymbol{p}}\}}{2m_e V}, \tag{5}$$

where $\hat{\sigma}_x$, $\hat{\sigma}_y$, and $\hat{\sigma}_z$ are the Pauli matrices, $\{.,.\}$ denotes the anti-commutator, V is a reference volume and k ($k = x, y, z$) an index specifying the direction of the spin polarization carried by the spin-current density. In this work, V refers to the individual atomic spheres, allowing us to compute atom-projected quantities (see Appendix A for details).

Using the linear-response formalism, we can compute the out-of-equilibrium electrically induced spin angular momentum $\delta\boldsymbol{S}$ as well as the induced spin-current density $\boldsymbol{J}^{S_k}$, using

$$\delta\boldsymbol{S} = \boldsymbol{\chi}^S\,\boldsymbol{E}, \tag{6}$$

$$\boldsymbol{J}^{S_k} = \boldsymbol{\sigma}^{S_k}\,\boldsymbol{E}, \tag{7}$$

where $\boldsymbol{\chi}^S$ is the spin ME susceptibility tensor and $\boldsymbol{\sigma}^{S_k}$ the spin conductivity tensor. Both $\boldsymbol{\chi}^S$ and $\boldsymbol{\sigma}^{S_k}$ are real 2nd-rank tensors, but note that, due to the spin component dependence, the spin conductivity tensor can be associated with a 3rd-rank tensor, $\boldsymbol{\sigma}^S$.

Analogous quantities can be straightforwardly defined for the orbital angular momentum $\hat{\boldsymbol{L}}$. Thus, we can define the orbital ME susceptibility tensor $\boldsymbol{\chi}^L$ and orbital conductivity tensor $\boldsymbol{\sigma}^{L_k}$,

$$\delta\boldsymbol{L} = \boldsymbol{\chi}^L\,\boldsymbol{E}, \tag{8}$$

$$\boldsymbol{J}^{L_k} = \boldsymbol{\sigma}^{L_k}\,\boldsymbol{E}, \tag{9}$$

where $\delta\boldsymbol{L}$ is the out-of-equilibrium electrically induced orbital angular momentum and $\boldsymbol{J}^{L_k}$ the induced orbital current density.

It is important to understand that the induced spin $\delta\boldsymbol{S}$ (orbital $\delta\boldsymbol{L}$) polarization and spin flow $\boldsymbol{J}^S$ (orbital flow $\boldsymbol{J}^L$) are correlated quantities. Just like the charge density and charge-density current, they are linked through the continuity equation. As our simulation cell is periodic in the in-plane x, y directions, in-plane flow of spin (orbital) current cannot lead to net spin (orbital) accumulation. Hence, an occurring nonzero δS_k (δL_k) can only be related to the spin (orbital) current density flowing along the symmetry-broken direction, i.e., to $J_z^{S_k}$ ($J_z^{L_k}$). In terms of response tensors, this translates into

the relationship

$$\chi_{kj}^{S(L)} \longleftrightarrow \sigma_{zj}^{S_k(L_k)}, \tag{10}$$

with j denoting the direction of the electric field $\boldsymbol{E}$. This association between $\chi_{kj}^{S(L)}$ and $\sigma_{zj}^{S_k(L_k)}$ will be extensively used in this paper as it offers insight, e.g. in how the SOT is related to spin and to spin currents.

3. Computational methodology

The bilayer structures that are studied here consist of several Pt monoatomic layers that are covered with two monoatomic layers of the $3d$ elements Ni, Co or Cu (see Fig. 1). For comparison, we also study the pure Pt system, where the top two monolayers consist of Pt. The nomenclature used in this deliverable is the following: we denote our systems by nPt/2Y where n is the total number of Pt monolayers and Y is either Ni, Co, Cu or Pt. The minimum total number of Pt monolayers used in our calculations is 2 while the maximum is 18 (denoted as 16Pt/2Pt). The maximum thickness achieved is then $\sim$3.2 nm. The direction normal to the interfaces is taken as the z axis. The monoatomic layers are labeled from $z = 1$ for the Pt monoatomic layer at the interface with vacuum (leftmost layer in Fig. 1) to $z = n + 2$ for the Y monoatomic layer at the interface with vacuum (rightmost layer in Fig. 1). Particular positions can be identified, like $z = n$ for the Pt monoatomic layer at the Pt/Y interface and $z = n + 1$ for the Y monoatomic layer at the Pt/Y interface.

To compute the spin and orbital susceptibility and conductivity tensors, we use the following three-step procedure.

1. The cell parameters and atomic positions of the heterostructures are fully relaxed with the DFT package SIESTA (Soler *et al.*, 2002).

2. Using the relaxed atomic positions, the ground-state Kohn-Sham wavefunctions and energies are selfconsistently computed with the accurate full-potential, all-electron DFT package WIEN2k (Blaha *et al.*, 2018).

3. Using the relativistic Kohn-Sham wavefunctions and energies, we compute the response tensors defined by Eq. (3).

As the DFT packages used employ full 3D periodic boundary conditions, all heterostructures contain 20 Å of vacuum to avoid spurious interactions with neighboring simulation cells.
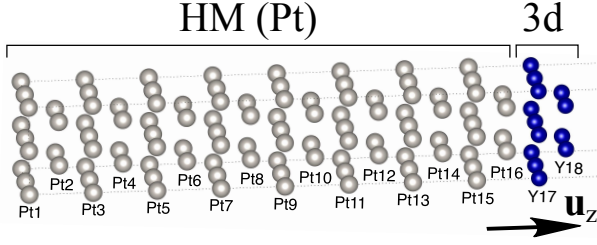
FIG. 1 Schematic of a typical system studied in this work, a nPt/$2Y$ bilayer. There are n ($=16$, here) monolayers of Pt heavy metal (HM) capped by two Y monolayers, where Y is Ni, Co, or nonmagnetic Cu or Pt. The z axis is taken normal to the slab, with unit vector $\boldsymbol{u}_z$. Each atomic plane is numbered with an index, where index 1 refers to the Pt atomic-layer interfaced with vacuum, n to the Pt atomic-layer interfaced with the 3d element in layer $n+1$, and $n+2$ labels the top layer at the vacuum interface.

4. Symmetry considerations

Before presenting calculated results it is instructive to consider the symmetry of the spin and orbital ME tensors. We start with considering the case where the equilibrium magnetization $\boldsymbol{M}$ is out-of-plane, i.e., $\boldsymbol{M} \parallel \boldsymbol{u}_z$. In this case, the computed $\boldsymbol{\chi}^S$ tensor can be written as

$$\boldsymbol{\chi}^S = \begin{pmatrix} \chi^S_{xx} & \chi^S_{xy} & 0 \\ \chi^S_{yx} & \chi^S_{yy} & 0 \\ 0 & 0 & \chi^S_{zz} \end{pmatrix} \quad [\boldsymbol{M} \parallel \boldsymbol{u}_z], \quad (11)$$

where furthermore $\chi^S_{xy} = -\chi^S_{yx}$ and $\chi^S_{xx} = \chi^S_{yy} \neq \chi^S_{zz}$. With $\boldsymbol{M}$ out-of-plane, the system exhibits an in-plane x/y spatial symmetry, which is fully recovered in our calculations. The $\boldsymbol{\chi}^S$ tensor can be further decomposed into an odd-in-$\boldsymbol{M}$ and even-in-$\boldsymbol{M}$ component,

$$\boldsymbol{\chi}^S(\boldsymbol{M}) = \boldsymbol{\chi}^S_o(\boldsymbol{M}) + \boldsymbol{\chi}^S_e(\boldsymbol{M}), \quad (12)$$

with specifically,

$$\boldsymbol{\chi}^S_e = \begin{pmatrix} 0 & \chi^S_{xy} & 0 \\ \chi^S_{yx} & 0 & 0 \\ 0 & 0 & 0 \end{pmatrix}, \quad (13a)$$

$$\boldsymbol{\chi}_o = \begin{pmatrix} \chi^S_{xx} & & 0 \\ 0 & \chi^S_{yy} & 0 \\ 0 & 0 & \chi^S_{zz} \end{pmatrix}. \quad (13b)$$

A nonzero odd-in-$\boldsymbol{M}$ part can obviously not exist for nonmagnetic systems (nPt/2Pt and nPt/2Cu), which is as well recovered in our calculations. The spin response is highly dependent on the magnetization direction. Setting the magnetization in plane, $\boldsymbol{M} \parallel \boldsymbol{u}_x$, the $\boldsymbol{\chi}^S$ tensor can

be written as

$$\boldsymbol{\chi}^S = \begin{pmatrix} 0 & \chi^S_{xy} & \chi^S_{xz} \\ \chi^S_{yx} & 0 & 0 \\ \chi^S_{zx} & 0 & 0 \end{pmatrix} \quad [\boldsymbol{M} \parallel \boldsymbol{u}_x], \quad (14)$$

clearly showing difference with the $\boldsymbol{M} \parallel \boldsymbol{u}_z$ case. Now the χ_{xy}, χ_{yx} elements are even-in-$\boldsymbol{M}$ and the χ_{xz}, χ_{zx} elements odd-in-$\boldsymbol{M}$. At this point we can furthermore mention already that the orbital $\boldsymbol{\chi}^L$ tensor has the same nonzero elements with the same $\boldsymbol{M}$ parity.

Next, depending on the relative orientation of the induced spin polarization $\delta\boldsymbol{S}$ with respect to (1) the applied electric field $\boldsymbol{E}$, (2) the normal direction $\boldsymbol{u}_z$ and (3) the equilibrium magnetization vector $\boldsymbol{M}$, the components of the ME susceptibility $\boldsymbol{\chi}^S$ can be classified according to three categories:

- $\boldsymbol{E}$-transverse components ($\boldsymbol{E}_\perp$):
$$\delta\boldsymbol{S} \propto \boldsymbol{E} \times \boldsymbol{u}_z, \quad (15)$$

- $\boldsymbol{M}$-transverse components ($\boldsymbol{M}_\perp$):
$$\delta\boldsymbol{S} \propto (\boldsymbol{E} \times \boldsymbol{u}_z) \times \boldsymbol{M}, \quad (16)$$

- $\boldsymbol{M}$-longitudinal component ($\boldsymbol{M}_\parallel$):
$$\delta\boldsymbol{S} \propto \boldsymbol{M} \text{ when } \boldsymbol{E} \propto \boldsymbol{u}_z. \quad (17)$$

For $\boldsymbol{M} \parallel \boldsymbol{u}_z$, we can directly associate these three categories with tensor elements: χ^S_{xy} and χ^S_{yx} are the $\boldsymbol{E}_\perp$ components, χ^S_{xx} and χ^S_{yy} are the $\boldsymbol{M}_\perp$ components, and χ^S_{zz} provides the $\boldsymbol{M}_\parallel$ component. A similar classification can be carried out for the case where $\boldsymbol{M} \parallel \boldsymbol{u}_x$. The classification and symmetry relations for the two considered magnetization directions are summarized for convenience in Table I. This classification will prove handy later on when we look at the magnetization direction dependence of $\boldsymbol{\chi}^S$, allowing us to map adequately the $\boldsymbol{M} \parallel \boldsymbol{u}_z$ and $\boldsymbol{M} \parallel \boldsymbol{u}_x$ cases on to each other.

C. Results

1. Spin response

a. *Magnetization out-of-plane.* We start with the case where $\boldsymbol{M} \parallel \boldsymbol{u}_z$. It is instructive to consider first the thickest heterostructures, i.e., 16Pt/2Ni, 16Pt/2Co, 16Pt/2Cu, and 16Pt/2Pt. In Figs. 2(a), (b), and (c) we show the computed atomic layer-resolved profiles of the aforementioned nonzero components of $\boldsymbol{\chi}^S$. As discussed earlier [see Eq. (10)], we can associate corresponding components of the spin conductivity tensor: $\sigma^{S_x}_{zy}$ and
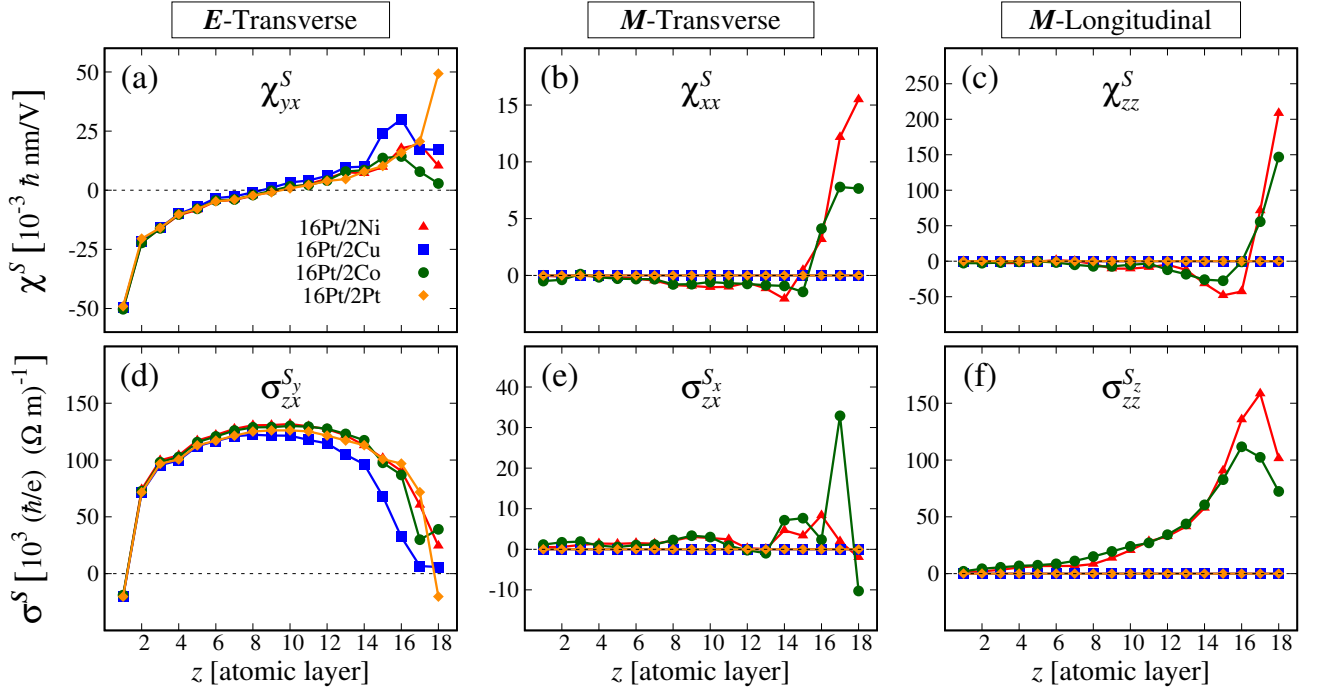
FIG. 2 Computed atomic layer-resolved nonzero components of the spin ME susceptibility $\boldsymbol{\chi}^S$ and spin conductivity $\boldsymbol{\sigma}^S$ of the 16Pt/2Y structures. (a) The $\boldsymbol{E}$-transverse component χ_{yx}^S, (b) $\boldsymbol{M}$-transverse component χ_{xx}^S, and (c) $\boldsymbol{M}$-longitudinal component χ_{zz}^S. The corresponding components of the spin conductivity tensor are given as (d) $\boldsymbol{E}$-transverse $\sigma_{zx}^{S_y}$, (e) $\boldsymbol{M}$-transverse $\sigma_{zx}^{S_x}$, and (f) $\boldsymbol{M}$-longitudinal $\sigma_{zz}^{S_z}$. The $\boldsymbol{E}$-transverse components can be associated with SHE. The $\boldsymbol{M}$-transverse components are nonzero only for magnetic systems (16Pt/2Ni and 16Pt/2Co) and in the vicinity of the interface, suggesting that those components arises from the Rashba spin-splitting of the electronic states and can thus be associated with the SREE. The $\boldsymbol{M}$-longitudinal components are discussed in the text. See Fig. 1 for the numbering of the atomic layers.

TABLE I The $\boldsymbol{E}$-transverse ($\boldsymbol{E}_\perp$), $\boldsymbol{M}$-transverse ($\boldsymbol{M}_\perp$), and $\boldsymbol{M}$-longitudinal ($\boldsymbol{M}_\parallel$) components of the $\boldsymbol{\chi}$ tensor for $\boldsymbol{M} \parallel \boldsymbol{u}_z$ and $\boldsymbol{M} \parallel \boldsymbol{u}_x$. Each row summarizes the equivalency of the $\boldsymbol{\chi}$ components for the two magnetization directions. The spatial symmetry relations as well as the symmetry with respect to $\boldsymbol{M}$ are also provided.

	$\boldsymbol{M} \parallel \boldsymbol{u}_z$	$\boldsymbol{M} \parallel \boldsymbol{u}_x$	Symmetry	$\boldsymbol{M}$-symmetry
$\boldsymbol{E}_\perp$	$\chi_{xy/yx}$	$\chi_{xy/yx}$	$\delta\boldsymbol{S} \propto \boldsymbol{E} \times \boldsymbol{u}_z$	$\boldsymbol{M}$-even
$\boldsymbol{M}_\perp$	$\chi_{xx/yy}$	χ_{zx}	$\delta\boldsymbol{S} \propto (\boldsymbol{E} \times \boldsymbol{u}_z) \times \boldsymbol{M}$	$\boldsymbol{M}$-odd
$\boldsymbol{M}_\parallel$	χ_{zz}	χ_{xz}	$\delta\boldsymbol{S} \propto \boldsymbol{M}, \boldsymbol{E} \propto \boldsymbol{u}_z$	$\boldsymbol{M}$-odd

$\sigma_{zx}^{S_y}$, respectively, to χ_{xy}^S and χ_{yx}^S, $\sigma_{zx}^{S_x}$ and $\sigma_{zy}^{S_y}$, respectively, to χ_{xx}^S and χ_{yy}^S, and $\sigma_{zz}^{S_z}$ to χ_{zz}^S. These spin conductivity elements are shown in Figs. 2(d), (e), and (f), respectively.

In all cases, we observe that the response of the Pt atomic-layer at the vacuum interface ($z = 1$) is virtually independent on the type of Y atom used, suggesting that these systems are thick enough to be able to isolate

the Pt/3d-interface properties. The inclusion of the two monoatomic layers of 3d elements mainly impacts the $\boldsymbol{\chi}^S$ and $\boldsymbol{\sigma}^S$ profiles close to their interface.

For the $\boldsymbol{E}$-transverse components (Figs. 2(a) and (d)), both $\boldsymbol{\chi}^S$ and $\boldsymbol{\sigma}^S$ are qualitatively barely impacted by the replacement of the two last Pt atomic monolayers by two 3d atomic monolayers. The profile of $\sigma_{zx}^{S_y}$ is in all cases mostly defined by a plateau in the center of the Pt layer. The spin-accumulation profile across the bilayer structure, as expressed by χ_{xy}^S/χ_{yx}^S, resembles strongly the type of spin accumulation that is expected from transverse spin flow due to the SHE (Stamm *et al.*, 2017; Zhang, 2000). Note that the accumulated spin moment is given by $\delta M = -2(\mu_B/\hbar)\delta S$, with μ_B the Bohr magneton. The specific component of $\boldsymbol{\sigma}^S$ is also the one identified as responsible for the SHE in Pt-bulk calculations. Reversing the magnetization of the Ni and Co layers from $+\boldsymbol{u}_z$ to $-\boldsymbol{u}_z$ in the calculations does not have a notable effect on the spin-accumulation given by χ_{yx}^S. This even-in-$\boldsymbol{M}$ symmetry is also in accordance with the magnetization independence of the SHE. Thus, these features strongly suggest that the $\boldsymbol{E}_\perp$ components are transport-driven and we therefore associate them to the SHE.
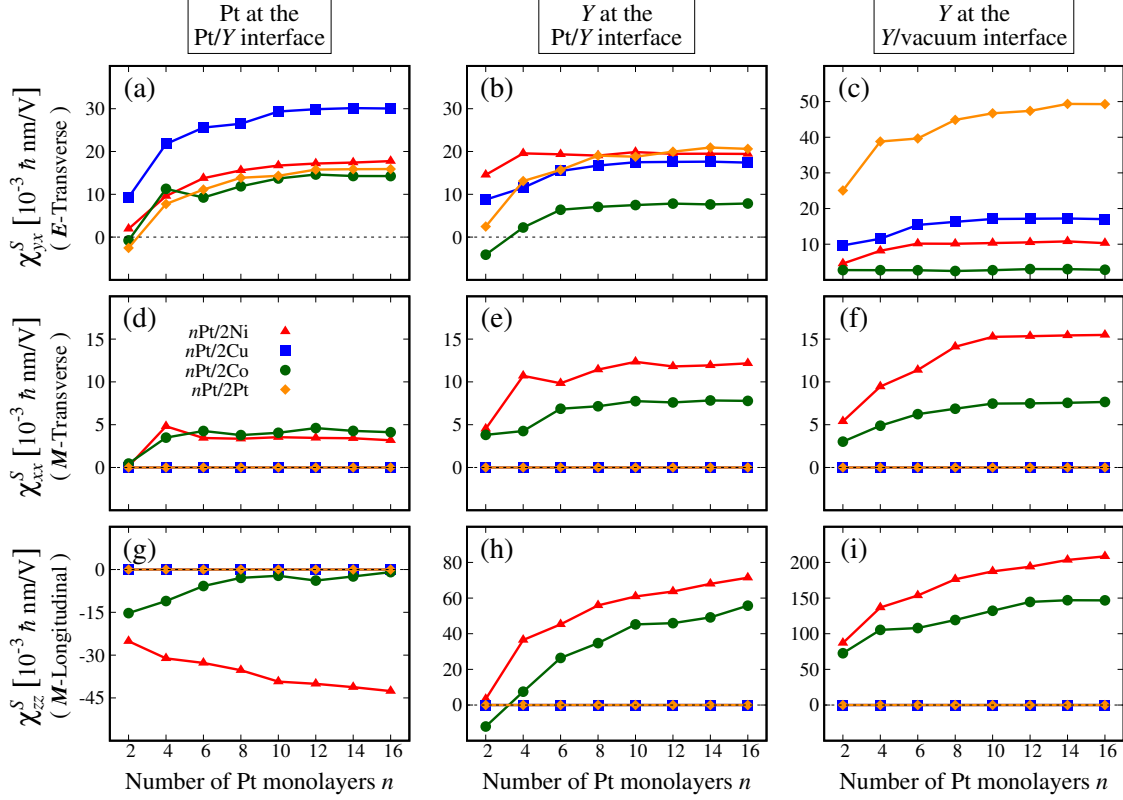
We further note that there is a small spin accumulation

FIG. 3 Dependence of the spin ME susceptibility tensor χ^S on the number of Pt monolayers n. Top row: $\boldsymbol{E}$-transverse component of χ^S, for (a) the Pt atom at the Pt/Y interface, (b) the Y atom at the Pt/Y interface, and (c) the Y atom at the Y/vacuum interface. Second row: $\boldsymbol{M}$-transverse component of χ^S, for (d) the Pt atom at the Pt/Y interface, (e) the Y atom at the Pt/Y interface, and (f) the Y atom at the Y/vacuum interface. Bottom row: $\boldsymbol{M}$-longitudinal component of χ^S, for (g) the Pt atom at the Pt/Y interface, (h) the Y atom at the Pt/Y interface, and (i) the Y atom at the Y/vacuum interface.

on the Pt-side of the Pt/Cu interface as well as a reduction of the spin accumulation in the top Cu monolayers, as compared to pure Pt (Fig. 2(a)). This illustrates a reduced spin transparency at the Pt/Cu interface. For 16Pt/2Ni and 16Pt/2Co one can in addition observe that a spin depolarization or spin loss occurs in the two ferromagnetic layers, as has been discussed in Refs. Dolui and Nikolić (2017); Kurt *et al.* (2003); Nguyen *et al.* (2014); Rojas-Sánchez *et al.* (2014); and Tao *et al.* (2018).

For the $\boldsymbol{M}$-transverse components (Figs. 2(b) and (e)), it is evident that sizable values are only obtained close to the interface with Co and Ni, both for χ^S and σ^S. Remarkably, while the $\boldsymbol{E}_\perp$ and $\boldsymbol{M}_\perp$ components are comparable in size close to the interface, their features differ greatly: (1) there is no bulk-like behavior for $\sigma_{zy}^{S_y}/\sigma_{zx}^{S_x}$, (2) those components are non-existent in bulk Pt, and (3) they are magnetization and magnetization direction dependent. Specifically, although there is a symmetry breaking at the Pt/Cu interface, no spin polarization is induced. These differences strongly suggest that the $\boldsymbol{M}$-transverse components are not related to spin transport from the bulk of the Pt layer to the interface, but rather to spin polarization generated at the spin-split interface. We therefore associate this component to the SREE. We note that our DFT Hamiltonian contains the full form of the spin-orbit interaction and is thus different from the more elementary Bychkov-Rashba SOC (Bychkov and Rashba, 1984), but it contains all materials' specific SOC effects.

The $\boldsymbol{M}$-transverse component is maximal for the Co and Ni atomic layers, but then it decays into the Pt film within ~ 8 atomic layers. Our calculation is consistent with that of Tokatly *et al.* (2015) who used a jelium model to study the SREE induced magnetization density in a Au slab.

The SHE leads to a spin accumulation in the $\boldsymbol{E}$-transverse direction that will exert a torque on the static magnetization $\boldsymbol{m}_0$ of the ferromagnetic layers, $\boldsymbol{m}_0 \times \delta \boldsymbol{S}$, acting here in the x direction, parallel to the electric field. The SREE, conversely, generates a spin polarization near the Pt/3d-metal interface in the direction of the $\boldsymbol{E}$ field, leading to a SOT exerted in the $\boldsymbol{E}_\perp$ direction, i.e., normal to the SOT due to the SHE.

The $\boldsymbol{M}$-longitudinal components, shown in Figs. 2(c)

and (f), are a bit peculiar in the sense that they are not directly SOT-related (the usual SOT configuration does not involve out-of-plane electrical fields and, also, no torque is generated by a spin accumulation parallel to the static moment). Though such components can be obtained via symmetry analysis (see Železný *et al.* (2017)), they haven't been, to the best of our knowledge, investigated so far. Nonetheless, as will be clarified further below, this effect is due to the spin-orbit interaction. Here, an electric field applied parallel to the out-of-plane magnetization causes a sign-changing spin polarization along $\boldsymbol{M}$ in the ~ 5 topmost monolayers. This is clearly a magnetic effect, as it does not exist for the nonmagnetic systems. The spin conductivity $\sigma_{zz}^{S_z}$ shows a decaying behavior from $z = 16$ to $z = 1$, but this decay is slower than that of the equilibrium spin magnetization in the systems. Also, similar to the $\boldsymbol{M}$-transverse component, no "bulk-like" behavior is observed, suggesting that the underlying mechanism of out-of-equilibrium spin generation is not linked to a SHE-induced spin transport. A possible way of observing this previously unidentified SOC-induced effect could be achieved by gating the ferromagnetic layer from the top and monitor a change of its magnetization.

So far, we focused on the components of the spin conductivity tensor giving rise to spin currents flowing along $\boldsymbol{u}_z$. While those components are the ones that should be of interest for understanding SOT in bilayer structures, other nonzero components can be observed, as well. For a magnetic system, we find that $\boldsymbol{\sigma^S}$ can generally be written as

$$\boldsymbol{\sigma^{S_x}} = \begin{pmatrix} 0 & 0 & \sigma_{xz}^{S_x} \\ 0 & 0 & \sigma_{yz}^{S_x} \\ \sigma_{zx}^{S_x} & \sigma_{zy}^{S_x} & 0 \end{pmatrix},$$

$$\boldsymbol{\sigma^{S_y}} = \begin{pmatrix} 0 & 0 & \sigma_{xz}^{S_y} \\ 0 & 0 & \sigma_{yz}^{S_y} \\ \sigma_{zx}^{S_y} & \sigma_{zy}^{S_y} & 0 \end{pmatrix}, \tag{18}$$

$$\boldsymbol{\sigma^{S_z}} = \begin{pmatrix} \sigma_{xx}^{S_z} & \sigma_{xy}^{S_z} & 0 \\ \sigma_{yx}^{S_z} & \sigma_{yy}^{S_z} & 0 \\ 0 & 0 & \sigma_{zz}^{S_z} \end{pmatrix}.$$

For a nonmagnetic system, $\sigma_{zx}^{S_x}$, $\sigma_{zy}^{S_y}$, and $\sigma_{zz}^{S_z}$ vanish.

The components associated to the SHE, i.e., $\sigma_{ij}^{S_k}$, where the indices are such that $\epsilon_{ijk} \neq 0$ (ϵ_{ijk} is the Levi-Civita symbol), are nonzero in all cases. However, while in cubic systems like bulk Pt they are all equal in magnitude, here, because of the symmetry breaking with respect to the z axis, the tensor elements are not invariant

under exchange of z and x or y indices.

The components $\sigma_{zx}^{S_x}$, $\sigma_{zy}^{S_y}$, and $\sigma_{zz}^{S_z}$, shown in Fig. 2, are the only odd-in-$\boldsymbol{M}$ components and therefore exists only for magnetic systems. Remarkably, the components $\sigma_{xz}^{S_x}$, $\sigma_{yz}^{S_y}$, $\sigma_{xx}^{S_z}$, and $\sigma_{yy}^{S_z}$ are even-in-$\boldsymbol{M}$ and thus exist for nonmagnetic systems. Those components emerge from the 2D character of our broken-symmetry systems. However, as discuss earlier, they do not contribute to the spin-orbit torque as they involve in-plane flow of spin angular momentum.

b. Pt-thickness dependence. As a next step, we investigate the Pt layer thickness dependence of the $\boldsymbol{E}_\perp$, $\boldsymbol{M}_\perp$, and $\boldsymbol{M}_\parallel$ components of $\boldsymbol{\chi}^S$. The number of Pt monolayers for our nPt/2Y systems is varied from $n = 2$ (Pt thickness ~ 0.38 nm) to $n = 16$ (Pt thickness ~ 3.08 nm). Figure 3 shows the computed Pt-thickness dependence where each column of the figure focuses on one particular atomic monolayer, with, from left to right, the Pt monolayer at the Pt/Y interface, the Y monolayer at the Pt/Y interface, and the Y atomic monolayer at the Y/vacuum interface. Each row focuses on one particular component, namely, from top to bottom, the $\boldsymbol{E}_\perp$, $\boldsymbol{M}_\perp$, and $\boldsymbol{M}_\parallel$ components. The values of the tensor elements that give rise to the SOT, the $\boldsymbol{E}_\perp$ and $\boldsymbol{M}_\perp$ components, barely fluctuate beyond $n = 8$ (Pt thickness ≥ 1.54 nm). Thus, both the SHE-driven and SREE-driven induced spin polarizations approach their maximum values already for relatively thin bilayers.

For the $\boldsymbol{E}_\perp$ components, in the case of pure Pt (nPt/2Pt), χ_{yx}^S tends to increase the closer we come to the last layer, which is typically what we would expect from a SHE-generated spin accumulation profile. When the two last layers are replaced by a magnetic element ($Y =$ Co or Ni) drastic changes occur. First, we observe that χ_{yx}^S is bigger for the 3d monolayer closer to the Pt layer than for the second Y layer, which can be interpreted as loss of the Pt generated spin accumulation in the Y layer. Second, at a fixed position, χ_{yx}^S is bigger for $Y =$ Ni than $Y =$ Co.

For the $\boldsymbol{M}_\perp$ components, representing the SREE response, the χ_{xx}^S for the Pt monolayer at the Pt/Y interface (Fig. 3(d)) is virtually identical for $Y =$ Ni or Co and for all Pt thicknesses considered, supporting that this is an interface-dominated effect. In the first and second magnetic monolayer (Figs. 3(e)) and (f)) the χ_{xx}^S is, in both cases, bigger for $Y =$ Ni than $Y =$ Co, predicting thus a larger induced Rashba-type spin polarization on Ni than on Co. The bottom row, lastly, shows the $\boldsymbol{M}$-longitudinal spin accumulation. Also here, we obtain that a larger magnitude of χ_{zz}^S is generated for $Y =$ Ni.

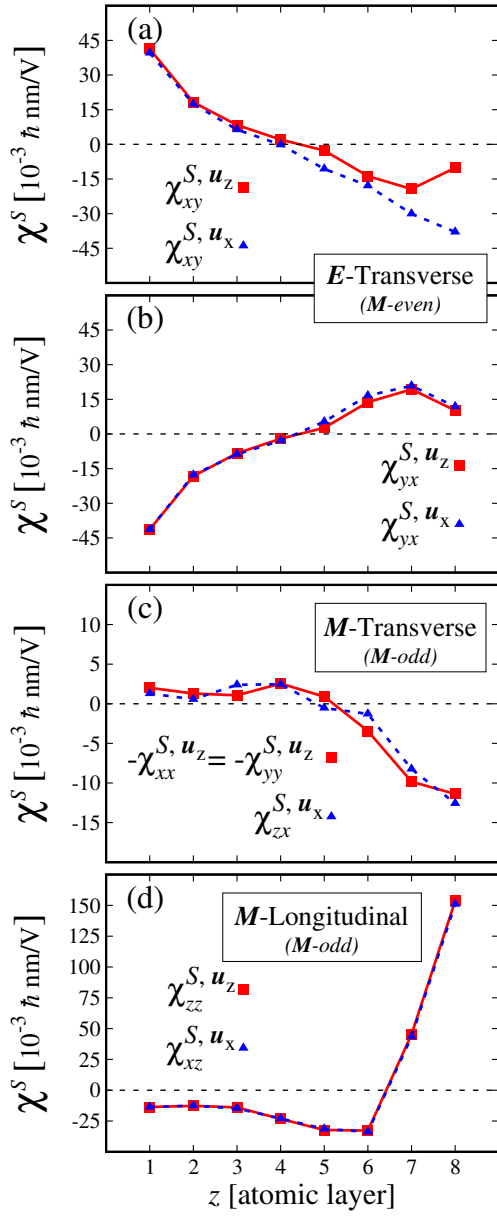*c. Magnetization-direction dependence.* The spin response is highly dependent on the magnetization direction. Set-

FIG. 4 Magnetization-direction dependence of the spin ME susceptibility tensor $\boldsymbol{\chi}^S$ for 6Pt/2Ni. Calculated data are given for $\boldsymbol{M} \parallel \boldsymbol{u}_z$ ($\boldsymbol{M} \parallel \boldsymbol{u}_x$) by the red squares (blue triangles). When the magnetization direction switches from $\boldsymbol{u}_z$ to $\boldsymbol{u}_x$, the transverse components $\chi_{xy}^{S,\boldsymbol{u}_z}$ and $\chi_{yx}^{S,\boldsymbol{u}_x}$ are mapped onto themselves, with χ_{xy}^S being notably modified close to the Pt/Ni interface while χ_{yx}^S is barely affected. The $\boldsymbol{M}$-transverse components $\chi_{xx/yy}^{S,\boldsymbol{u}_z}$ are mapped onto $-\chi_{zx}^{S,\boldsymbol{u}_x}$. The $\boldsymbol{M}$-longitudinal $\chi_{zz}^{s,\boldsymbol{u}_z}$ component is transformed onto $\chi_{xz}^{S,\boldsymbol{u}_x}$.
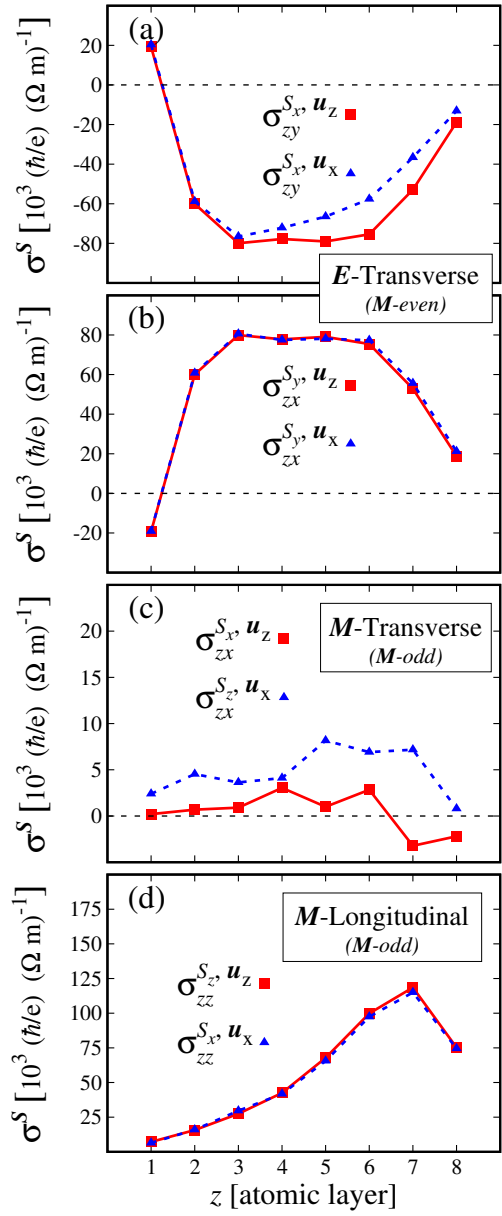
FIG. 5 Magnetization-direction dependence of the spin conductivity tensor $\boldsymbol{\sigma}^{\boldsymbol{S}}$ for 6Pt/2Ni. The calculated data are given for magnetization $\boldsymbol{M} \parallel \boldsymbol{u}_z$ ($\boldsymbol{M} \parallel \boldsymbol{u}_x$) by the red squares (blue triangles). Computed spin conductivity tensor elements are given for (a) the $\boldsymbol{E}$-transverse conductivities, (b) the $\boldsymbol{M}$-transverse conductivities, and (c) the $\boldsymbol{M}$-longitudinal components. The correspondence between the calculated $\boldsymbol{M} \parallel \boldsymbol{u}_z$ and $\boldsymbol{M} \parallel \boldsymbol{u}_x$ components show that the analytic transformation relations are obeyed.

ting the magnetization in plane ($\boldsymbol{M} \parallel \boldsymbol{u}_x$), the $\boldsymbol{\chi}^S$ tensor

can be written as

$$\boldsymbol{\chi}^S = \begin{pmatrix} 0 & \chi_{xy}^S & \chi_{xz}^S \\ \chi_{yx}^S & 0 & 0 \\ \chi_{zx}^S & 0 & 0 \end{pmatrix}, \qquad (19)$$

clearly being different from the $\boldsymbol{M} \parallel \boldsymbol{u}_z$ case (see Eq. (11)).

Using the symmetry relations defined in Eqs. (15), (16), and (17), we can easily track how individual tensor components are transformed when the $\boldsymbol{M}$ direction is changed. The transformation relations between the two cases, as well as the symmetry relations, are summarized for convenience in Table I.

To simplify our discussion, we use the superscript $\boldsymbol{u}_z$ ($\boldsymbol{u}_x$) when discussing quantities computed with $\boldsymbol{M} \parallel \boldsymbol{u}_z$ ($\boldsymbol{M} \parallel \boldsymbol{u}_x$). In Fig. 4 and Fig. 5 we show $\boldsymbol{\chi}^S$ and $\boldsymbol{\sigma}^S$, respectively, for 6Pt/2Ni, both for $\boldsymbol{M} \parallel \boldsymbol{u}_x$ and $\boldsymbol{M} \parallel \boldsymbol{u}_x$. It is crucial to understand that we discuss the *equivalence* of components as quantitative differences may appear.

The pair $\chi_{xy}^{S,\boldsymbol{u}_z} / \chi_{xy}^{S,\boldsymbol{u}_x}$, shown in Fig. 4(a), differs the most, especially close to the Pt/Ni interface. This is the component that is driven by the SHE-generated spin current; the difference can be explained as follows. The polarization of the spin current generated by $\sigma_{zy}^{S_x,\boldsymbol{u}_x}$ is parallel to $\boldsymbol{M}$ while it is perpendicular to $\boldsymbol{M}$ for $\sigma_{zy}^{S_x,\boldsymbol{u}_z}$. We should therefore expect a drastic change in spin transparency and the spin conductivities $\sigma_{zy}^{S_x,\boldsymbol{u}_x} / \sigma_{zy}^{S_x,\boldsymbol{u}_z}$ of the Pt/Ni interface (see Fig. 5(a)). The spin transparency of a ferromagnetic layer is typically small for a perpendicular spin direction (Ghosh *et al.*, 2012). Moreover, this observation also explains why no difference is observed for the pair $\chi_{yx}^{S,\boldsymbol{u}_z} / \chi_{yx}^{S,\boldsymbol{u}_x}$: the polarization of the spin current generated by $\sigma_{zx}^{S_y,\boldsymbol{u}_x}$ is perpendicular to $\boldsymbol{M}$, just like for $\sigma_{zx}^{S_y,\boldsymbol{u}_z}$. The same behavior can be observed for the two related spin conductivities $\sigma_{zx}^{S_y,\boldsymbol{u}_x}$ and $\sigma_{zx}^{S_y,\boldsymbol{u}_z}$ in Fig. 5(b).

As mentioned before, the spin-conductivity elements $\sigma_{ij}^{S_k}$ are nonzero for indices such that $\epsilon_{ijk} \neq 0$. The interchange of two of the indices leads then to a sign change, as can be observed for the components shown in Figs. 5(a) and (b).

While the mapping for the $\boldsymbol{E}_\perp$ components for $\boldsymbol{M} \parallel \boldsymbol{u}_z$ and $\boldsymbol{M} \parallel \boldsymbol{u}_x$ is trivial, the practicality of the symmetry relations appears when one considers $\boldsymbol{M}_\perp$ and $\boldsymbol{M}_\parallel$. Indeed, the mapping using symmetry relations allows us to pick up a possible sign reversal. As displayed in Fig. 4(c), the $\boldsymbol{M}_\perp$ components are equal in magnitude but opposite in sign. Using the symmetry relations, one finds for the corresponding tensor components

$$\chi_{xx}^{\boldsymbol{u}_z} \to \delta \boldsymbol{S} \propto (\boldsymbol{u}_x \times \boldsymbol{u}_z) \times \boldsymbol{u}_z = -\boldsymbol{u}_x,$$

while for $\boldsymbol{M} \parallel \boldsymbol{u}_x$ we have,

$$\chi_{zx}^{\boldsymbol{u}_x} \to \delta \boldsymbol{S} \propto (\boldsymbol{u}_x \times \boldsymbol{u}_z) \times \boldsymbol{u}_x = +\boldsymbol{u}_z,$$

which perfectly captures the sign reversal. The deviation for the $\boldsymbol{M}$-transverse conductivity components in Fig. 5(c) appears as somewhat larger, but note that the absolute values of the conductivities are ten times smaller. Lastly, the $\boldsymbol{M}$-longitudinal $\boldsymbol{\chi}^S$ and σ_{zz}^S components obey

the mapping properties quite well, see Figs. 4(d) and 5(d). Note that these "hidden" tensor components remain hidden when $\boldsymbol{M}$ is rotated from $\boldsymbol{u}_z$ to $\boldsymbol{u}_x$.

2. Orbital response

a. Dependence on magnetization direction. A similar analysis can be performed for the orbital response, both in terms of $\boldsymbol{\chi}^L$ and $\boldsymbol{\sigma}^L$. While similarities are observed, unique characteristic can be observed, too, for $\boldsymbol{\chi}^L$ and $\boldsymbol{\sigma}^L$. We show in Fig. 6 the calculated layer-resolved orbital ME susceptibilities $\boldsymbol{\chi}^L$ and orbital conductivities $\boldsymbol{\sigma}^L$ for the 16Pt/2Y systems, similar to the spin counterparts shown in Fig. 2.

The layer-resolved results, shown in Fig. 6, reveal that, just like for the spin, the $\boldsymbol{E}$-transverse component resembles strongly the transport-induced accumulation of orbital angular momentum. Therefore, we identify this component as being due to the OHE. Notwithstanding the analogy to the spin response, the overall shapes of χ_{yx}^L and $\sigma_{zx}^{L_y}$ show distinct features when compared to their spin counterparts. The overall shape the χ_{yx}^L profile is considerably less smooth and the flat plateau for $\sigma_{zx}^{L_y}$ in the center of the Pt layer is far more extended. Notably, considering the values obtained, we obtain a huge orbital response χ_{yx}^L, roughly one order of magnitude larger than the spin counterpart. This finding is consistent with previous calculations of the OHE in bulk metals, which obtained an intrinsic OHE that is much larger than the SHE (Jo *et al.*, 2018; Kontani *et al.*, 2009; Tanaka *et al.*, 2008).

A further distinction with respect to the spin response is the extended flat area of $\sigma_{zx}^{L_y} / \sigma_{zy}^{L_x}$ in the interior of the Pt layer where the orbital susceptibility, and thus the local accumulated orbital polarization, vanishes.

When it comes to the relative magnitude of the different contributions, also strikingly differences compared to the spin response can be observed. Here, the response at the interface is dominated by the $\boldsymbol{E}$-transverse component. Since we associate this component, as before, to transport and therefore to the OHE, our calculations show how gigantic the contribution from the OHE is. The $\boldsymbol{M}$-transverse and $\boldsymbol{M}$-longitudinal orbital ME susceptibilities (Figs. 6(b) and (c)), are an order of magnitude smaller. Again, it is evident that the latter two orbital susceptibilities have a purely magnetic origin as they vanish for the nonmagnetic systems and are furthermore caused by the breaking of inversion symmetry. Similarly to the case of the spin angular momentum, we identify the $\boldsymbol{M}$-transverse component χ_{xx}^L therefore as being due to the OREE. The nonequilibrium orbital polarizations induced by the OHE and the OREE are perpendicular to one another, just as we found for the SHE and SREE. However, as the OHE is much larger than the
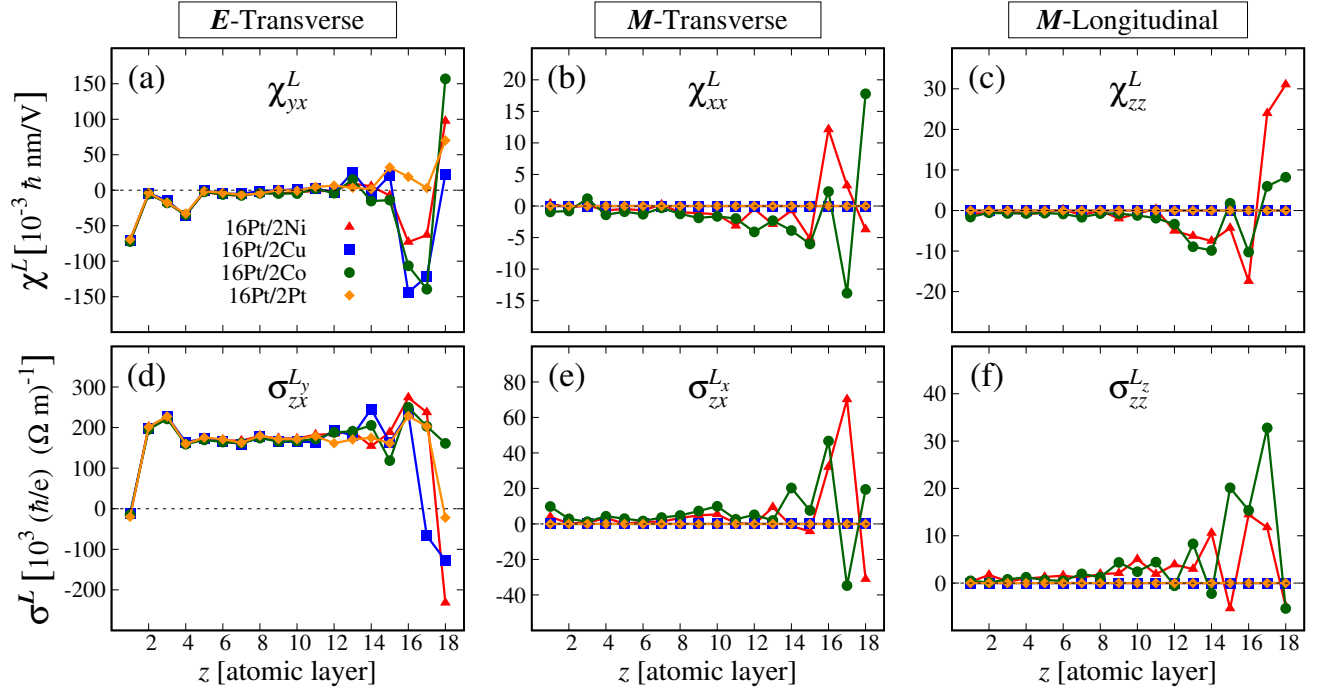
FIG. 6 Atomic layer-resolved nonzero components of the orbital ME susceptibility $\boldsymbol{\chi}^L$ and the orbital conductivity $\boldsymbol{\sigma}^L$ of the 16Pt/2Y films with $\boldsymbol{M} \parallel \boldsymbol{u}_z$. (a) The $\boldsymbol{E}$-transverse component χ_{yx}^L, (b) $\boldsymbol{M}$-transverse component χ_{xx}^L, and (c) the $\boldsymbol{M}$-longitudinal component χ_{zz}^L. The corresponding components of the orbital conductivity tensor are given as (d) $\boldsymbol{E}$-transverse $\sigma_{zx}^{L_y}$, (e) $\boldsymbol{M}$-transverse $\sigma_{zx}^{L_x}$, and (f) $\boldsymbol{M}$-longitudinal $\sigma_{zz}^{L_z}$. The $\boldsymbol{E}$-transverse components are associated with the OHE, conventionally defined for bulk Pt. The $\boldsymbol{M}$-transverse components are nonzero only for the magnetic systems (16Pt/2Ni and 16Pt/2Co) and are associated with the OREE. The $\boldsymbol{M}$-longitudinal components also arise from the spin polarization of the electronic states.

OREE, the induced orbital angular momentum will be dominantly due to nonlocal flow and not to generation at the symmetry-broken interface. A further significant difference between the spin and orbital ME susceptibilities is the rapid variation of the orbital ME susceptibilities in the last few layers of the Pt/Y interface. While the χ_{yx}^S (SHE) component has positive values for the monolayers in the vicinity of the interface (Fig. 2(a)), the orbital counterpart exhibits a sign change for the two topmost layers. This implies that any resulting orbital torque on the static moments in these layers will also point in opposite directions. A similar behavior can be observed for the $\boldsymbol{M}$-transverse components, χ_{xx}^S and χ_{xx}^L. The unusual $\boldsymbol{M}$-longitudinal components exist, too, for the orbital ME susceptibility and conductivity, Figs. 6(c) and (f), but these quantities are much smaller than their spin counterparts.

Pt-layer thicknesses of about 8 monolayers provide stable values for the OH and OREE components of the the orbital ME susceptibilities.

The dependence of the orbital response $\boldsymbol{\chi}^L$ on the magnetization direction shows similarities with the spin response $\boldsymbol{\chi}^S$, as the nonzero components are the same for both cases. However, while the pair $\chi_{xy}^{S,\boldsymbol{u}_z}/\chi_{xy}^{S,\boldsymbol{u}_x}$ differs

close to the Pt/Ni interface, we find that $\chi_{xy}^{L,\boldsymbol{u}_z}/\chi_{xy}^{L,\boldsymbol{u}_x}$ are virtually identical. This indicates a different, much smaller, dependence of orbital transport on the magnetization direction at an interface. Currently, orbital transport at interfaces is only poorly understood, and first measurements are being made (Ding *et al.*, 2020; Kim *et al.*, 2020). Our calculations indicate that orbital transparency at the interface is not really affected by the magnetization direction.

b. Dependence on spin-orbit coupling. To investigate the dependence of the spin and orbital ME susceptibilities and conductivities we can vary the the strength of the spin-orbit coupling in the calculations. To do this, we artificially introduce a SOC scaling parameter α in the DFT calculations such that $\hat{H}_0$ can be written as $\hat{H}_0 = \hat{H}_{\text{sc}} + \alpha\hat{H}_{\text{soc}}$ where $\hat{H}_{\text{sc}}$ is the scalar-relativistic part of the Hamiltonian and $\hat{H}_{\text{soc}}$ the SOC part. Doing so, we find that the $\hat{H}_{\text{soc}}$ term is *necessary* in order to observe a nonzero spin ME susceptibility and spin conductivity, i.e., setting $\alpha = 0$ gives us $\boldsymbol{\chi}^S = 0$ and $\sigma_{ij}^{S_k} = 0$, with indices such that $\epsilon_{ijk} \neq 0$. Thus, these spin quantities are completely induced by the SOC. For $\boldsymbol{\chi}^L$, the story is
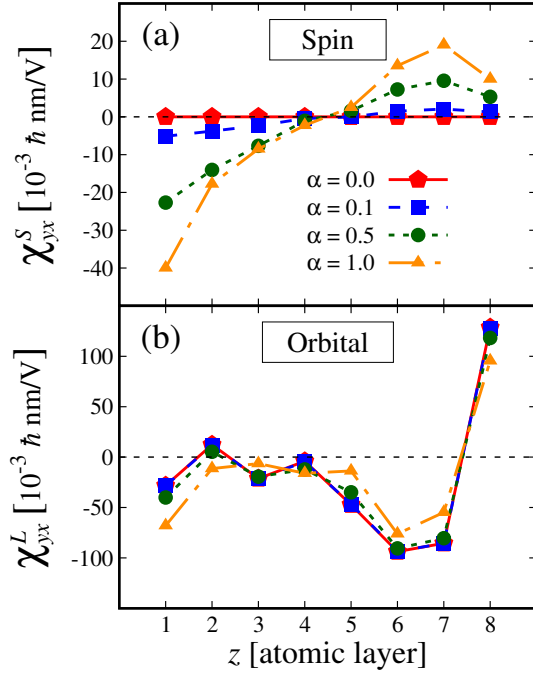
FIG. 7 Scaling behavior of (a) χ^S_{yx}, and (b) χ^L_{yx} as a function of the SOC scaling parameter α, calculated for the 6Pt/2Ni system. The $\boldsymbol{E}_\perp$ component of the spin ME susceptibility (a) scales with α, and represents a SOC-induced quantity. The $\boldsymbol{E}_\perp$ component of the orbital ME susceptibility (b) exists even without SOC.

quite different. When α is set to zero, χ^L_{xy} and χ^L_{xy}, as well as their associated $\boldsymbol{\sigma}^L$ components, are present and actually no really affected by the modified SOC strength, a feature of the OHE that has been noted before (Kontani *et al.*, 2009; Tanaka *et al.*, 2008).

In Fig. 7 we show comprehensive results for the layer-resolved profile of χ^S_{xy} and χ^L_{xy} for 6Pt/2Ni, computed for $\alpha = 0$, 0.1, 0.5, and 1, with $\alpha = 1$ corresponding to the intrinsic SOC strength. It is evident from Fig. 7(a) that spin ME susceptibility is a pure SOC effect that scales linearly with the SOC. The situation is different for the orbital ME susceptibility, which exhibits practically no dependence on the SOC strength, see Fig. 7(b). For all other spin and orbital susceptibility components, as well as their related spin and orbital conductivity tensors, we find that these scale with the size of the SOC, i.e., these are quantities induced by the SOC.

D. Discussion

1. Spin-orbit torque

Freimuth *et al.* (2015) evaluated directly the SOT using a different approach to the perturbative framework. While our computational method differs from theirs, we can evaluate the SOT $\mathcal{T}_{\text{SOT}}$ in a similar fashion. The

torque $\mathcal{T}_{\text{SOT}}$ is defined as

$$\mathcal{T}_{\text{SOT}} = \boldsymbol{m}_0 \times \boldsymbol{B}_{\text{SOT}}, \qquad (20)$$

where $\boldsymbol{m}_0 = -2(\mu_B/\hbar)\boldsymbol{S}_0$ is the equilibrium magnetization of spin angular momentum $\boldsymbol{S}_0$ in an atomic layer, and $\boldsymbol{B}_{\text{SOT}}$ the electrically-induced effective SOT magnetic field. We can evaluate $\boldsymbol{B}_{\text{SOT}}$ as

$$\boldsymbol{B}_{\text{SOT}} \approx \frac{\delta \boldsymbol{S}}{|\boldsymbol{S}_0|} \frac{\langle V^\downarrow_{\text{KS}} - V^\uparrow_{\text{KS}}\rangle}{2\mu_B}, \qquad (21)$$

where $\delta \boldsymbol{S}$ is the induced spin angular momentum and $V^\downarrow_{\text{KS}}$ ($V^\uparrow_{\text{KS}}$) the Kohn-Sham effective potential for minority (majority) spin electrons. The SOT effective magnetic field $\boldsymbol{B}_{\text{SOT}}$ can also be written as

$$\boldsymbol{B}_{\text{SOT}} = \underbrace{\frac{\langle V^\downarrow_{\text{KS}} - V^\uparrow_{\text{KS}}\rangle}{2\mu_B|\boldsymbol{S}_0|} \chi^S}_{\chi_{\text{SOT}}} \boldsymbol{E}, \qquad (22)$$

where we define $\boldsymbol{\chi}_{\text{SOT}}$ as the SOT spin susceptibility tensor in units of $[\text{TmV}^{-1}]$. Since our computational approach involves quantities evaluated for each atomic site, we can access a layer-resolved $\boldsymbol{B}_{\text{SOT}}$.

For the thickest magnetic systems, 16Pt/2Co and 16Pt/2Ni, we find that the SHE-driven $\boldsymbol{E}_\perp$ contribution to the SOT at the first (second) layer of Ni is 0.0032 (0.0020) mTcmV^{-1} and 0.0019 (0.0007) mTcmV^{-1} for Co. For the SREE-driven $\boldsymbol{M}_\perp$ contribution, we find 0.0020 (0.0030) mTcmV^{-1} for the first (second) layer of Ni and 0.0019 (0.0020) mTcmV^{-1} the first (second) layer of Co. These values are smaller than, but consistent with, those obtained by Freimuth *et al.* (2014), because they used a much smaller broadening of electronic states.

It is in principle possible to compute in a similar way values for the torque due to the orbital susceptibility. Although the torque value one could obtain through the OHE might seem large, the induced orbital polarization can only couple to the static magnetic spin moment $\boldsymbol{m}_0$ via SOC, which puts it back on the same footing as the SOT due to current-induced spin polarization. It remains thus a question for future studies how important the orbital torque is. Currently, theoretical efforts are devoted to predicting the orbital torque (Go *et al.*, 2020; Go and Lee, 2020) and experimental efforts are being devoted to detecting the orbital torque and disentangling it from the spin torque (Chen *et al.*, 2018; Tazaki *et al.*, 2020).

2. Relative size of Hall and Rashba-Edelstein coefficients

Associating the SHE (OHE) to the $\boldsymbol{E}_\perp$ components of $\boldsymbol{\chi}^S$ ($\boldsymbol{\chi}^L$) and the SREE (OREE) to the $\boldsymbol{M}_\perp$ components, we quantify the relative importance of the two effect by
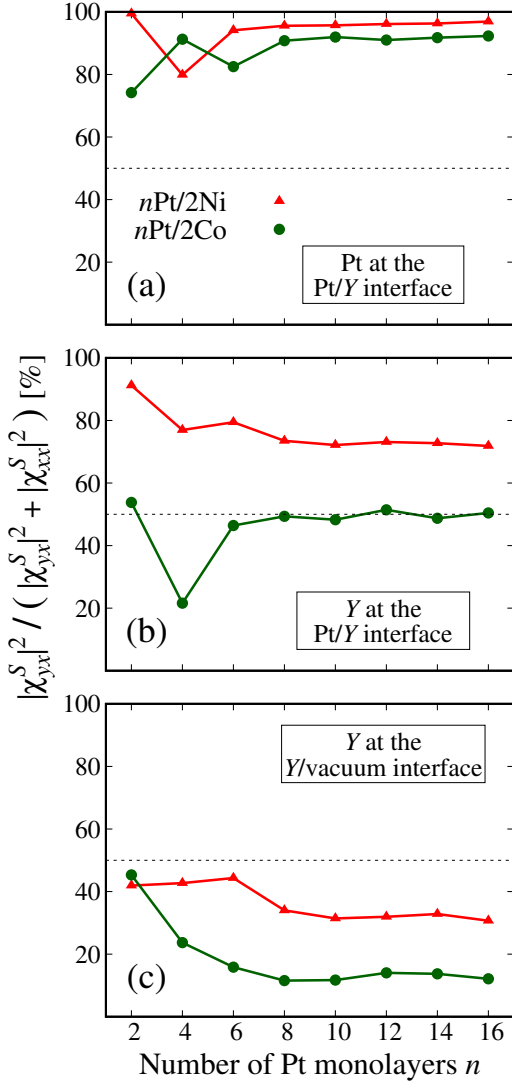
FIG. 8 Computed ratio of the $\boldsymbol{E}$-transverse SHE component χ_{yx}^{S} to the total (vectorial summed) SHE and SREE (χ_{xx}^{S}) components as function of Pt layer thickness. (a) The ratio at the Pt atom at the Pt/Y interface, (b) the ratio at the Y atom at the Pt/Y interface, and (c) at the Y atom at the Y/vacuum interface.

computing the ratio

$$\frac{|\chi_{xy}^{S(L)}|^2}{|\chi_{xy}^{S(L)}|^2 + |\chi_{xx}^{S(L)}|^2} \cdot 100\% \tag{23}$$

A value of $> 50\%$ ($< 50\%$) would then refer to an SHE dominated (SREE dominated) origin of the torque. The square exponent accounts for the fact that we are comparing vectorial quantities. Note that $|\chi_{xx}^{S(L)}|$ should be replaced by $|\chi_{zx}^{S(L)}|$ for $\boldsymbol{M} \parallel \boldsymbol{u}_x$.

The calculated Pt-thickness dependence of this ratio for the SHE and SREE is displayed in Fig. 8. There is virtually no change for the computed ratio for Pt

layer thicknesses beyond eight Pt monolayers. For the Pt monolayer at the Pt/Y interface, the induced torque is to 90% composed of the SHE component, see Fig. 8(a). For the Y monolayer at the Pt/Y interface, the torque consists for $\sim 75\%$ of the SHE component for $Y = $ Ni and $\sim 50\%$ for $Y = $ Co (Fig. 8(b)). For the Y monolayer at the Y/vacuum interface, the torque consist for $\sim 30\%$ of the SHE component for $Y = $ Ni and $\sim 10\%$ for $Y = $ Co (Fig. 8(c)). This suggests that the Pt/Ni interface is more transparent to spin currents from the Pt than the Pt/Co interface, consistent with the better matching electronic structures of isoelectronic fcc Ni and Pt. Thus, the THz emission from Ni/Pt could be larger as well. On the other hand, the moment of Co is larger than that of Ni, and thus the superdiffusive spin current generated by demagnetization of Co can be larger than that generated in Ni. The torques resulting from the induced spin polarization on the two ferromagnetic Y monolayers will be the most important ones for the magnetization switching. The torque on the ferromagnetic layer at the vacuum interface is thus dominated by the SREE, whereas the torque at the ferromagnetic layer adjacent to the Pt layer has a larger contribution from the SHE. As the relative contribution of the $\boldsymbol{E}_\perp$ and $\boldsymbol{M}_\perp$ components differs in both $3d$ monolayers, the direction of the total torque per monolayer will be different for each of the two Y monolayers. Any resulting layer-resolved torque can, as customary done, be decomposed in a fieldlike component, $\propto \boldsymbol{m_0} \times \delta\boldsymbol{S}$, and a dampinglike component, $\propto \boldsymbol{m_0} \times (\boldsymbol{m_0} \times \delta\boldsymbol{S})$. The calculated atomic-layer specific torques are ideally suited to investigate current-driven magnetization switching dynamics using atom-specific Landau-Lifshitz-Gilbert spin-dynamics simulations (see e.g. Evans *et al.* (2014); Jungfleisch *et al.* (2017); and Nowak (2007)). Such simulations would provide insight in how the magnetization of the ferromagnetic layers reverses and even allow for a dependence of the torques on the magnetization direction.

An equivalent ratio can be computed for the OHE and the OREE. However, for the orbital case this ratio is of the order of 99% as it is completely dominated by the OHE-driven component which is much larger than the OREE-driven one (and therefore not shown explicitly).

E. Summary

We have employed first-principles calculations to investigate the electric-field induced spin and orbital magneto-electric susceptibility and the spin and orbital conductivity of heavy-metal/$3d$-metal bilayer structures. For each orientation of the $3d$ magnetization and the applied electric field we have shown that the susceptibility tensor and its associated conductivity tensor can be uniquely decomposed in components depending on the spatial symmetries, i.e., transverse electric $\boldsymbol{E}_\perp$, transverse magnetic

$M_\perp$, and longitudinal magnetic components $M_\parallel$, as well as the magnetic symmetries (odd-in-M and even-in-M, respectively). Our atomic-layer specific calculations of the tensors show that all components are highly dependent on the position of the atomic layer in the considered heterostructure.

Analyzing the properties of the computed ME susceptibilities, we have identified the even-in-M, $E_\perp$-components of χ^S as spin accumulation associated with the SHE and the odd-in-M, $M_\perp$-components associated with the SREE. Extending the calculations to field-induced orbital polarization, we have performed a similar analysis and decomposition for the orbital susceptibility tensor χ^L and orbital conductivity, σ^L. We have analyzed the relative importance of the different spin and orbital contributions as a function of Pt thickness. Both the SHE-driven and SREE-driven out-of-equilibrium spin responses lead to atomic-layer dependent SOTs that are of the same order of magnitude, but act in perpendicular directions. We find that the spin accumulation due to the SHE is largest for the Pt layer at the Pt/$3d$-metal interface. The SREE is larger at the $3d$-vacuum interface. Our calculations show that both effects should be considered together when analyzing current-induced spin polarization in heavy-metal/ferromagnetic bilayer systems.

For the electric-field induced orbital polarization we find that the orbital susceptibility and conductivity components corresponding to the OHE are always much larger ($\sim 10\times$) than those corresponding to the OREE, as the OHE is barely dependent on SOC. Although the OHE is sizable, it can however only couple to the equilibrium spin moment via SOC.

Our calculations show furthermore that there exists as well an electric-field induced spin and orbital polarization along the magnetization direction. This previously unobserved spin-orbit effect does not exert a torque on the static magnetization. We propose that it could be possible to observe this M-longitudinal effect in sensitive magneto-optical Kerr effect measurements (cf. Stamm *et al.* (2017)).

When the magnetization direction changes, the spin and orbital responses also change. We have shown that the magnetization direction does have a strong influence on the spin and orbital responses, but that it is possible to track the evolution of the individual components using simple, but robust, symmetry relations. This should aid the investigation of SOT magnetization switching using atom-specific Landau-Lifshitz-Gilbert spin-dynamics simulations.

II. SPIN AND ORBITAL RASHBA-EDELSTEIN COEFFICIENTS OF NONCENTROSYMMETRIC CUMNAS AND MN$_2$AU

A. Introductory remarks

AFM SOT-based electrical detection of THz radiation is in the focus of WP2, specifically, in T2.2 and T2.3. Among the AFM materials of choice are the noncentrosymmetric metallic AFMs CuMnAs and Mn$_2$Au. The SOT in these materials is quite special. Since CuMnAs and Mn$_2$Au do not have a spacial center of inversion in their AFM structure, it has been proposed that there exists a staggered SOT on the AFM moments that is due to the Rashba-Edelstein effect (Wadley *et al.*, 2016; Železný *et al.*, 2014). This staggered SOT is as yet only poorly understood. To obtain a better understanding of how spin accumulation due to the REE can lead to a SOT, we have performed detailed *ab initio* calculations of the REE in these materials. In addition we investigate this charge-to-spin conversion in the full frequency domain. The results of the investigation were published recently (Salemi *et al.*, 2019).

Although previously disregarded, AFMs have recently emerged as appealing candidate materials for information processing devices since they offer various advantages (Baltz *et al.*, 2018; Jungwirth *et al.*, 2016; Němec *et al.*, 2018). Specifically, AFMs are robust against external magnetic field perturbations, they are available as insulators, semiconductors and metals, allowing thus for versatile environment integration, and they often have a high Néel temperature (Barthem *et al.*, 2013; Máca *et al.*, 2012; Yamaoka, 1974), suitable for room-temperature operation of the devices. Moreover, their intrinsic spin dynamics is ultrafast, in the THz domain (Fiebig *et al.*, 2008; Kampfrath *et al.*, 2010; Kimel *et al.*, 2004) (compared to GHz dynamics reported for ferromagnets (Kirilyuk *et al.*, 2010; Pashkin *et al.*, 2013)).

The efficient manipulation of the magnetization of materials remains a crucial challenge in the field of spintronics (Brataas *et al.*, 2012; Hellman *et al.*, 2017; Žutić *et al.*, 2004). Achieving efficient control over the magnetization in antiferromagnets is however an even more complicated issue. For ferromagnets, the SHE has proven to generate a spin-polarized current (Kato *et al.*, 2004b; Sinova *et al.*, 2015) and create an SOT that can act efficiently on the magnetization of a ferromagnetic layer (Baumgartner *et al.*, 2017; Garello *et al.*, 2013; Liu *et al.*, 2012; Miron *et al.*, 2011). The SREE can induce a nonequilibrium spin polarization in solids lacking inversion symmetry (Edelstein, 1990).

More recently, the REE has been proposed as a method to create a current-induced staggered spin polarization and SOT in the noncentrosymmetric antiferromagnets CuMnAs and Mn$_2$Au (Barthem *et al.*, 2013; Wadley *et al.*, 2015, 2013) causing the antiferromagnetic mag-

netic moments to flip to a perpendicular direction (Bodnar *et al.*, 2018; Godinho *et al.*, 2018; Meinert *et al.*, 2018; Olejník *et al.*, 2017, 2018; Wadley *et al.*, 2016). These recent experiments indicate that current driven switching of the Néel vector is possible, however, the operation of the SOT and the switching path are not understood yet. Microscopic investigations indicate that a complex switching process with both domain wall motion and domain flips may occur (Grzybowski *et al.*, 2017; Wadley *et al.*, 2018). It is moreover a question how large the induced staggered moments are. So far, linear-response tight-binding calculations with Rashba SOC (Železný *et al.*, 2017, 2014) and an *ab initio* calculation (Wadley *et al.*, 2016) of the current induced magnetic fields have been performed, that however differed considerably. Also a semiclassical model based on the Boltzmann equation has been employed to compute the induced magnetization in a Weyl semimetal (Johansson *et al.*, 2018). These investigations focused moreover on the induced spin polarization and neglect any possible contribution stemming from an induced orbital magnetization.

In this Section we investigate computationally the full magnetic polarization induced by a time-varying applied electric field in the noncentrosymmetric antiferromagnets CuMnAs and Mn$_2$Au. Our DFT-based calculations bring insights into the Rashba-Edelstein effect in these antiferromagnets. We show that the dominant contribution to the induced polarizations stems from the OREE. The OREE tensor can have a symmetry different from that of the SREE tensor (e.g., Rashba vs. Dresselhaus-type of symmetry). Due to the pronounced Rashba symmetry of the OREE tensor, a strong orthogonal orbital-momentum locking is obtained for in-plane electric fields. We find furthermore that quite sizable moments can be electrically induced on the nonmagnetic atoms. Investigating the origin of the large induced orbital polarizations, we show that these are present even without spin-orbit interaction, whereas the SREE tensor is proportional to the SOC and vanishes without SOC, signifying that the latter are induced through the relativistic SOC, whereas the former have a nonrelativistic origin.

B. Results

1. Theoretical framework

We use linear-response theory to evaluate the magnetic response to a time-dependent electric field $\boldsymbol{E}(t)$. The induced magnetic polarization $\delta\boldsymbol{M} = \mu_B\delta(\boldsymbol{L}+2\boldsymbol{S})$, consisting of orbital ($\boldsymbol{L}$) and spin ($\boldsymbol{S}$) contributions, reads in the frequency domain

$$\delta M_i(\omega) = \sum_j \left[\chi_{ij}^L(\omega) + 2\chi_{ij}^S(\omega)\right] E_j(\omega), \qquad (24)$$

where $\chi_{ij}^L(\omega)$ and $\chi_{ij}^S(\omega)$ ($i, j = x$, y, or z) are the OREE and SREE susceptibility tensor, respectively (in units of $\mu_B\,\mathrm{nm}\,\mathrm{V}^{-1}$). For the response-theory expressions for the OREE and SREE tensors see Sec. I B 1.

To evaluate the frequency-dependent SREE and OREE tensors, we adopt the DFT formalism as implemented in the full-potential linearized augmented plane-wave (FLAPW) all-electron code WIEN2k (Blaha *et al.*, 2018). For details of the computational approach, see Sec. I B 1. In the following we apply this framework to noncentrosymmetric CuMnAs and Mn$_2$Au that have recently drawn attention for antiferromagnetic spintronics (Baltz *et al.*, 2018; Bodnar *et al.*, 2018; Jungwirth *et al.*, 2016; Meinert *et al.*, 2018; Olejník *et al.*, 2018; Wadley *et al.*, 2016).

2. Results for CuMnAs

Our DFT calculations give that CuMnAs has an antiferromagnetic ground state with Mn atoms carrying a magnetic moment of ∼3.66 μ_B, in agreement with recent experiments (Wadley *et al.*, 2015, 2013). The tetragonal cell of CuMnAs (space group $P4/nmm$), shown in Fig. 9(a), consists of six inequivalent atoms, two of each chemical species. Both the Mn and As atoms have the $4mm$ point group whereas the Cu atoms possess the $-4m2$ point group symmetry. The magnetic ordering is such that adjacent {001} Mn planes are antiferromagnetically coupled while Mn atoms laying in the same plane are ferromagnetically ordered. The As atoms are also found to carry a small magnetic moment of ∼2.33 10^{-3} μ_B. Their orientation is such that {001} As planes are ferromagnetically coupled to the closest {001} Mn plane. The Cu atoms are found to be nonmagnetic.

The AFM moments can orient along different Néel vector axes and this direction of the AFM moments depends sensitively, for thin films, on the interplay of intrinsic magneto-crystalline anisotropy and shape anisotropy. Experimentally, an orientation of the spins in the *ab*-plane has been observed for thin films (Wadley *et al.*, 2015).

The SREE and OREE tensors depend on the orientation of the moments. We compute them here for different orientations of the moments, and in addition, we compute the atom-resolved tensors' spectra, using a specific labeling of the atoms as shown in Fig. 9(a).

We first consider the case where magnetic moments are oriented along the *c*-axis and the applied field is along the *a*-axis (Fig. 9(a)). This magnetic configuration does not break the 4-fold rotational symmetry about the *c*-axis (hard magnetization axis). The real parts of the nonzero components of the atom-resolved spin and orbital Rashba-Edelstein tensors are displayed in Fig. 9(d). Several remarkable observations can now be made. First, there are frequency-dependent induced
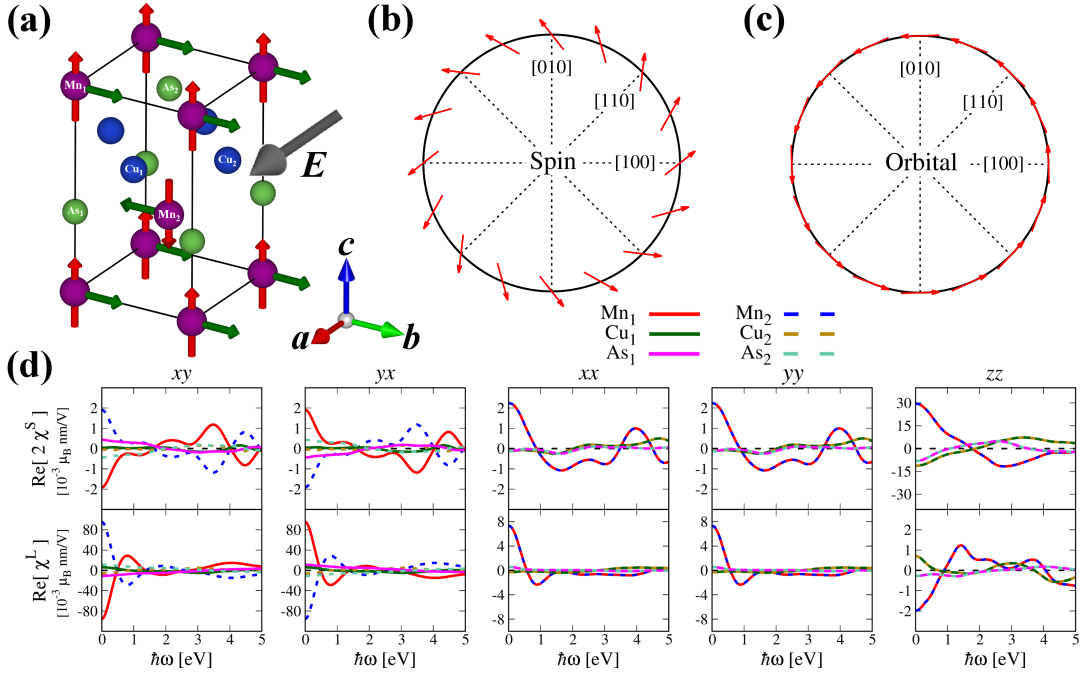
FIG. 9 Magnetization induced by the Rashba-Edelstein effect in AFM CuMnAs. **(a)** Sketch of the tetragonal unit cell of CuMnAs with the magnetic moments constrained to the *c*-axis. The inset depicts the direction of the crystal axes. The red arrows on the manganese atoms represent the initial magnetic moments. Applying an electric field $\boldsymbol{E}$ along the (100) direction (grey arrow) induces a non-equilibrium magnetization mainly along the (010) direction (green arrows). **(b)** Symmetry of the induced spin magnetization as a function of the static electric field direction for Mn_1. **(c)** Symmetry of the induced orbital magnetization as a function of the static electric field direction for Mn_1. **(d)** Real parts of the nonzero tensor components (labeled ij, with $i, j = x$, y or z) of the SREE and OREE susceptibilities, $Re[2\chi^S]$ and $Re[\chi^L]$, as function of frequency, $\hbar\omega$.

moments not only on the Mn atoms, but also on the Cu and As atoms. Second, the orbital contribution that was thus far disregarded, is not negligible. In fact the staggered orbital part χ^L_{xy} is the dominating part of the response and is ∼45 times larger than its spin counter part at $\omega = 0$. In the near-infrared region ($\hbar\omega = 0.6$ to 1.2 eV) χ^L_{xy} dominates even more, since the spin response χ^S_{xy} is quite small. Third, apart from the staggered components, that are such that antiferromagnetic Mn_1 and Mn_2 atoms experience an opposite response (off-diagonal xy and yx), there are also homogeneous induced components that act in the same direction for a given atomic species (see diagonal diagonal xx, yy and zz tensors elements in Fig. 9(d)). These non-staggered induced longitudinal magnetizations are not small, especially for the spin response, and can alter the atomic torques and influence eventual spin switching. Lastly, we note that SREE and OREE tensors of the individual elements obey different symmetries, specific to the atomic site's point group. For the Mn atoms we observe $\chi^{S,L}_{xy} = -\chi^{S,L}_{yx}$, and $\chi^{S,L}_{xx} = \chi^{S,L}_{yy}$. The same symmetry of the tensors is obtained for the As atoms, but for the Cu atoms $\chi^{S,L}_{xy} = \chi^{S,L}_{yx}$ and $\chi^{S,L}_{xx} = \chi^{S,L}_{yy}$.

The calculated orientation of the induced moments as a function of the direction of an in-plane applied static electric field is displayed in Figs. 9(b), (c) for the spin

and orbital part, respectively. We observe a Rashba-like behavior for the spin part with nonorthogonal spin-momentum locking, whereas the orbital part possesses a nearly perfect Rashba symmetry with orthogonal orbital-momentum locking; for a definition, see e.g. Ciccarelli *et al.* (2016) and Manchon *et al.* (2015). These plots are obtained by computing the tensors at $\omega = 0$ while varying the direction of $\boldsymbol{E}$. It is important to note that the induced spin and orbital moments depend on the frequency ω. In addition, the fact that the spin and orbital polarization are induced in different directions, and can even be antiparallel (see below) has an important consequence. The resultant torque field that acts on the atomic moments in a Landau-Lifshitz-Gilbert spin-dynamics formulation can then not be represented in the form of a single atomic Zeeman field, corresponding to an interaction $(\mu_B/\hbar)(\hat{\boldsymbol{L}} + 2\hat{\boldsymbol{S}}) \cdot \boldsymbol{H}$, with $\boldsymbol{H}$ the applied atomic Zeeman magnetic field, as this would lead to a proportional induced spin and orbital atomic moment.

We now consider the case of CuMnAs with an in-plane magnetization along the (100) direction which corresponds to the magnetic structure realized in experiments. As shown in Fig. 10(a), applying a static electric field (grey arrow) along the magnetization direction (red arrows) induces magnetic moments (green arrows) mainly on the Mn atoms. Those magnetic moments are
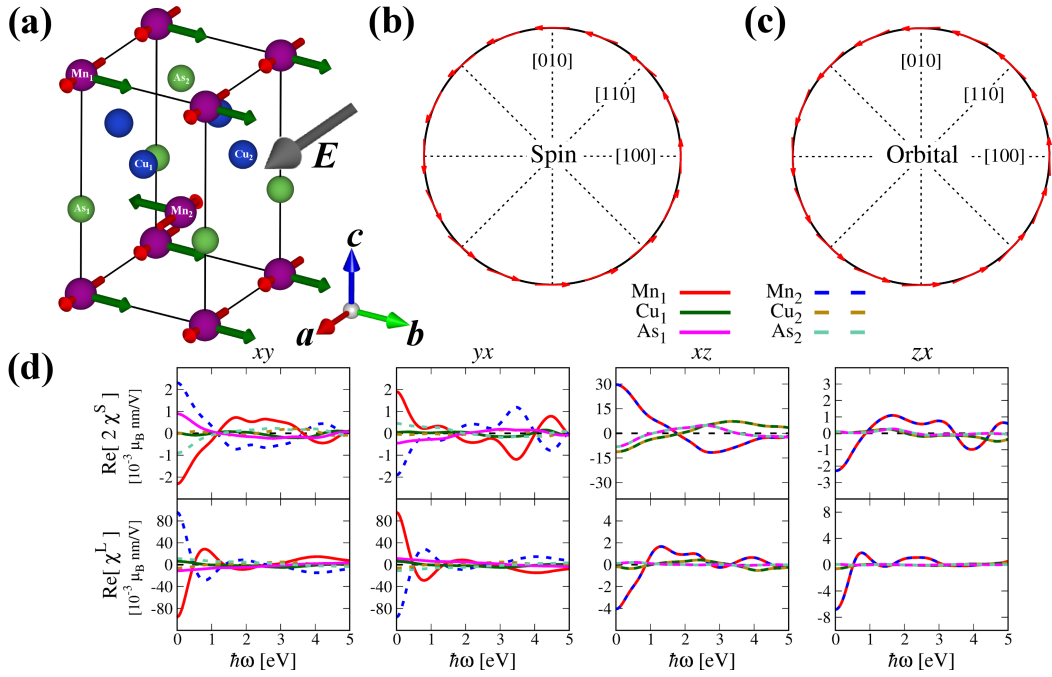
FIG. 10 Rashba-Edelstein effect in CuMnAs with magnetic moments along the a-axis. **(a)** Sketch of the tetragonal unit cell of CuMnAs. The red arrows on the Mn atoms represent the initial magnetic moments. Applying an electric field $\boldsymbol{E}$ along the (100) direction (grey arrow) induces a nonequilibrium magnetization mainly along the (010) direction (green arrows). **(b)** In-plane symmetry of the induced spin magnetization as a function of the static electric field direction for Mn_1. **(c)** In-plane symmetry of the induced orbital magnetization as a function of the static electric field direction for Mn_1. **(d)** Real parts of the nonzero components ij ($i, j = x$, y or z) of the SREE and OREE susceptibility tensors, $Re[2\chi^S]$ and $Re[\chi^L]$.

staggered, i.e., they are practically antiparallel to each other for AFM coupled Mn atoms. However, a parallel out-of-plane contribution is also present. This non-staggered feature of the magnetic response can be recognized by looking at the SREE and OREE tensors, shown in Fig. 10(d). Especially the nonzero χ^S_{zx} tensor component gives a non-staggered contribution. Nonetheless, the by far dominant part of the induced magnetic polarization is again contained in the staggered xy and yx components of the orbital response.

Another important point to be noticed is that the nonzero homogeneous tensor components have changed with the changed direction of the Néel vector. The non-staggered components for CuMnAs with magnetization along (001) were the diagonal xx, yy, and zz components while for the magnetization along (100), these are the xz and zx components. As can be seen in Figs. 9(d) and 10(d), the computed SREE spectra are very similar, with an inverted sign ($\chi^S_{zz} \longrightarrow \chi^S_{xz}$, and $\chi^S_{xx} \longrightarrow -\chi^S_{zx}$). This is a direct demonstration that the electrically induced magnetization texture depends on the underlying magnetization direction itself. This can be understood as an influence of the magnetization direction on the eigenstates which affects the induced magnetization (Železný *et al.*, 2017). This effect has also been observed experimentally in (Ga,Mn)As (Kurebayashi *et al.*, 2014). Computing the symmetry of the momentum-dependent induced spin and

orbital polarizations for an in-plane static electric field, we find that both the spin- and orbital resolved parts exhibit a Rashba symmetry (Figs. 10(b), (c)). Here, it can be recognized that the induced spin and orbital polarizations cooperate and exert spin and orbital torques in the same direction. We further note that the symmetries of the REE tensor are now such that $\chi^S_{xy} \neq -\chi^S_{yx}$, but $\chi^L_{xy} = -\chi^L_{yx}$ for the Mn and As atoms. The latter tensor elements are the largest, which illustrates the dominance of the OREE.

3. Results for Mn_2Au

Mn_2Au crystallizes in the tetragonal structure shown in Fig. 11(a) ($I4/mmm$ space group). The ground state of Mn_2Au is computed to be antiferromagnetic with magnetic moments of 3.69 μ_B only on the manganese atoms. Experimentally, the magnetization of Mn_2Au films is found to lie in {001} (basal) planes, with ∼4 μ_B moments on Mn (Barthem *et al.*, 2013). The unit cell consists of two equivalent Au atoms and two pairs of inequivalent Mn atoms, labeled Mn_1 and Mn_2 in Fig. 11(a). The four Mn atoms have the $4mm$ (polar) point group symmetry and the two Au atoms have the $4/mmm$ (centrosymmetric) point group symmetry.
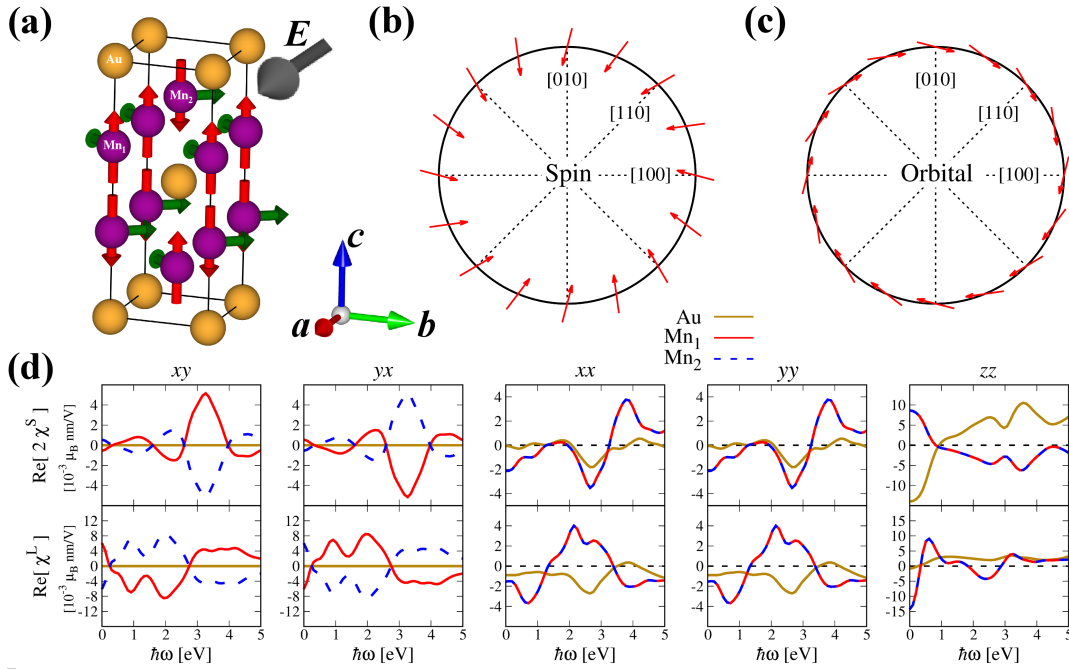
Figure 11(d) shows the real parts of the nonzero SREE

FIG. 11 Rashba-Edelstein effect in Mn_2Au with magnetic moments along the c-axis. **(a)** The unit cell of Mn_2Au, with red arrows on the Mn atoms depicting the initial magnetic moments. Applying an electric field E along the (100) direction (grey arrow) induces a non-equilibrium magnetization tilted in between the (010) and (100) direction (green arrows). **(b)** Symmetry of the induced spin magnetization as a function of the static electric field direction for Mn_1. **(c)** Symmetry of the induced orbital magnetization as a function of the static electric field direction for Mn_1. **(d)** Real parts of the nonzero components ij ($i, j = x, y$ or z) of the SREE and OREE susceptibilities, $\mathrm{Re}[2\chi^S]$ and $\mathrm{Re}[\chi^L]$, as function of electric field frequency, $\hbar\omega$.

and OREE tensor elements, computed for Mn moments along the c-axis. The calculated tensors exemplify that the REE of Mn_2Au is in several aspects different from that in CuMnAs. The spin and orbital responses for both the xy and yx components are staggered in Mn_2Au and the homogeneous part of the response is in the diagonal xx, yy and zz components, similar to CuMnAs. The orbital part of the response is not as dominant as in the case of CuMnAs. The largest orbital contribution in the off-diagonal elements is almost 12 times larger than the spin contribution for $\omega = 0$. We can furthermore observe that the non-magnetic Au atoms do not display any finite staggered response, consistent with the centrosymmetric nature of its point group $4/mmm$.

The directional dependence of the current-induced moments on Mn atoms as a function of the direction of an in-plane applied static electric field is shown in Figs. 11(b) and 11(c) for the spin and orbital response, respectively. The spin response exhibits a Rashba-like behavior and the orbital counterpart possesses a Rashba-like symmetry, too, but notably practically in a direction perpendicular to that of the spin response. Hence, for any applied in-plane field, the current-induced spin and orbital moments will exert torques in perpendicular directions during a switching process.

We now consider Mn_2Au with moments laying in the ab-plane along the (100) direction, see Fig. 12(a). As

for CuMnAs, the magnetic moments have been experimentally found to lie in the ab-plane (Barthem *et al.*, 2013). Here, the calculated nonzero REE tensor elements are the xy, yx, xz and zx components. The real parts of the nonzero Rashba-Edelstein tensor elements are shown in Fig. 12(d). In this configuration, the staggered responses for both spin and orbital contributions are present in the xy and yx components whereas the non-staggered responses are present in the zx and xz components, that however give smaller contributions. The mainly staggered response corroborates the investigation of Železný *et al.* (2014) who predicted staggered spin-orbit fields on the two Mn sublattices. The symmetries of the main staggered tensor elements are $\chi^S_{xy} \neq -\chi^S_{yx}$ but $\chi^L_{xy} = -\chi^L_{yx}$, as we also obtained for CuMnAs with Néel vector along the a-axis.

Considering the symmetry of the induced polarizations for an in-plane field in Fig. 12(b), (c), we find that the SREE exhibits a Dresselhaus-type behavior and the OREE exhibits a pure Rashba symmetry. Again, the possible non-cooperativity of the OREE and SREE when exerting a torque can be fully recognized. When both the static moments and electric field are along the a-axis ([100]) the induced spin and orbital magnetizations are antiparallel and the torques will partially compensate each other. For an in-plane electric field E along the b-axis the orbital and spin magnetizations do not counter-
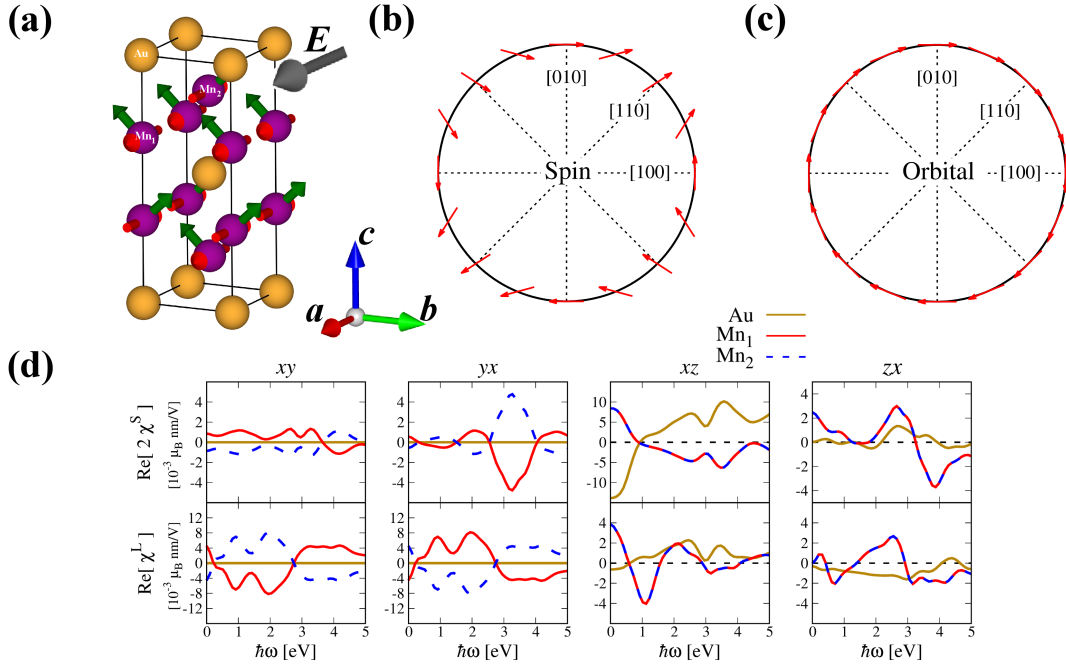
FIG. 12 Rashba-Edelstein effect in Mn_2Au with magnetic moments along the a-axis. **(a)** The unit cell of Mn_2Au. The red arrows on the Mn atoms represent the initial magnetic moments. Applying an electric field $\boldsymbol{E}$ along the (100) direction (grey arrow) induces a nonequilibrium magnetization mainly along the (010) direction (green arrows). **(b)** In-plane symmetry of the induced spin magnetization as a function of the static electric field direction for Mn_1. **(c)** Symmetry of the induced orbital magnetization as a function of the static electric field direction for Mn_1. **(d)** Real parts of the nonzero tensor components ij ($i, j = x, y$ or z) of the SREE and OREE susceptibilities, $\mathrm{Re}[2\chi^S]$ and $\mathrm{Re}[\chi^L]$, as function of the electric field frequency, $\hbar\omega$.

act each other (see also Fig. 12(d)), but this configuration only leads to an induced longitudinal moment along the static AFM moments that does not exert a local torque on the atomic moment. This exemplifies that devising optimal SOT switching conditions can be quite intricate.

C. Discussion

1. Importance of spin-orbit interaction

In his original work, Edelstein predicted an electrically induced out-of-equilibrium spin magnetization generated by Rashba SOC (Edelstein, 1990). Here, without assuming any specific shape for the SOC, we find that, depending on the magnetic configuration, the symmetry of the induced magnetization can adopt Rashba-like or Dresselhaus-like behaviors. Remarkably, we find that the previously neglected orbital polarization can in fact be much larger than the induced spin polarization. The possible existence of an induced orbital magnetization has been suggested in earlier studies (Boiko and Rashba, 1960; Levitov *et al.*, 1985).

The importance of SOC on the magnetoelectric susceptibilities can be accessed by reducing or switching off SOC in the calculations. The results of these calculations are shown in Fig. 13. We find that the spin Rashba-

Edelstein effect computed without SOC completely vanishes; therefore, consistent with Edelstein's model (Edelstein, 1990), this is an intrinsic effect which occurs due to the broken local inversion symmetry in the presence of SOC. Surprisingly, however, for the orbital component our calculations without SOC give an unchanged, non-vanishing OREE response for the dominant off-diagonal tensor elements. In Fig. 13(a), (b) we show the computed SOC dependence of the xx and xy tensor elements of the SREE susceptibility of Mn_1 in CuMnAs with antiferromagnetic moments along the c-axis. These elements decrease linearly with decreasing SOC. For the OREE, we find that the staggered components χ_{xy}^L, shown in Fig. 13(d), and χ_{yx}^L (not shown), are present even without SOC, and are not even changed by SOC strength which suggests that the leading off-diagonal term is independent of SOC. In contrast, without SOC the non-staggered OREE components χ_{xx}^L, shown in Fig. 13(c), as well as χ_{yy}^L and χ_{zz}^L (not shown) vanish, and these can consequently be identified as intrinsic SOC-related quantities. This observation is quite crucial and unexpected, since the staggered SREE components are generally believed to be at the origin of switching, in e.g. CuMnAs, and to be SOC related. We find that the dominant nonrelativistic contribution is in the staggered OREE components while smaller staggered spin components and non-staggered or-
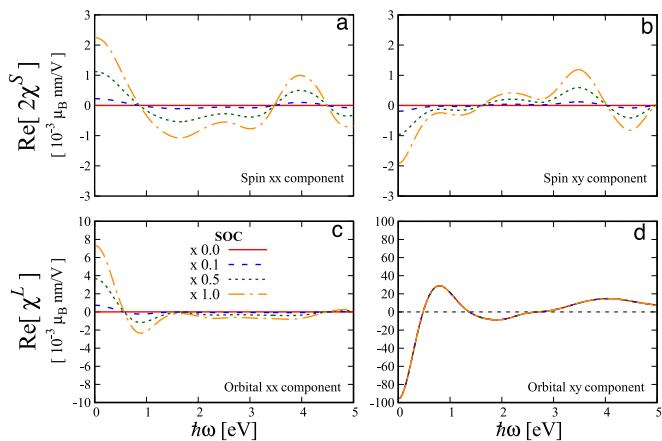
FIG. 13 Rashba-Edelstein effect as a function of SOC strength. Calculated results are given for the Mn_1 atom of AFM CuMnAs with moments along the c axis, for scaled values of the SOC, as given in the legend. (a), (b) Results for the $Re[\chi^S_{xx}]$ and $Re[\chi^S_{xy}]$ component, respectively, of the SREE susceptibility tensor. (c), (d) Results for the $Re[\chi^L_{xx}]$ and $Re[\chi^L_{xy}]$ component of the OREE tensor, respectively, as function of electric field frequency $\hbar\omega$.

bital components are generated by SOC.

As yet we know little about the influence of the OREE for a magnetization switching event, but a cautioning remark is warranted. Although the OREE can be large, to act on the spin moments present in an AFM, it needs to couple to these through spin-orbit interaction. Then, the overall torque on the antiferromagnetic spin moments will eventually be proportional to the SOC.

To analyze the origin of the induced orbital polarizations, we observe that due to the staggered nature of the induced moments in Fig. 11, the sum of the induced orbital moments on all atoms in the unit cell cancels, but the contributions on individual atoms do not. There is thus an atomic orbital polarization present even without SOC. The orbital angular momentum dynamics induced by the applied potential $\hat{V}(t) = -e\,\boldsymbol{E}(t)\cdot\hat{\boldsymbol{r}}$, where e is the electron charge and $\hat{\boldsymbol{r}}$ the position operator, can be evaluated from the Heisenberg expression in a single-electron picture as

$$\frac{d\hat{\boldsymbol{L}}^{\mathrm{ind}}}{dt} = -\frac{\mathrm{i}}{\hbar}\left[\hat{\boldsymbol{L}}^{\mathrm{ind}}, \hat{V}(t)\right] = \hat{\boldsymbol{r}} \times e\,\boldsymbol{E}(t), \qquad (25)$$

which is the quantum mechanical counter-part of the classical equation of motion for angular momentum, $\frac{d\boldsymbol{L}}{dt} = \boldsymbol{r} \times \boldsymbol{F}$, where $\boldsymbol{F}$ is an externally applied force. In this picture, the electric field acts as a torque on the center of mass of the electrons on an atom. The current-induced nonequilibrium electron populations provide then a nonzero atomic orbital polarization, similar to the nonequilibrium Fermi surface shift leading to spin-orbit torques (Kurebayashi *et al.*, 2014). This mechanism does not require the interplay of SOC as the field couples di-

rectly to the position of the electrons and thereby affects the orbital momentum. Therefore, the OREE does not arises only from the small relativistic SOC, and sizeable effects might thus even be observed in systems with small SOC.

A symmetry analysis adds further insight to the appearance of the orbital texture even without SOC. In the crystal structure of antiferromagnetic tetragonal CuMnAs inversion symmetry $\mathcal{P}$ and time-reversal symmetry $\mathcal{T}$ are broken, but $\mathcal{PT}$ symmetry is obeyed. The antiferromagnetic Mn atoms Mn_1 and Mn_2 are inversion partners under $\mathcal{PT}$ symmetry (Wadley *et al.*, 2016). Using $\mathcal{P}$ and $\mathcal{T}$ transformation properties, $\mathcal{PT}\{L^{\mathrm{ind}}_{Mn_1}\} = -L^{\mathrm{ind}}_{Mn_2}$ and vice versa, i.e., $\mathcal{PT}$ symmetry enforces the nonzero orbital moments to be staggered. Even with vanishing equilibrium spin moments the two Mn atoms are inversion symmetry partners and, interestingly, $\mathcal{PT}$ symmetry enforces the induced orbital polarizations to be staggered as well in the nonmagnetic phase.

We furthermore point out that the here-observed appearance of an orbital polarization in the unit cell in the absence of SOC is distinct from other recent theoretical predictions of nonzero orbital textures (Go *et al.*, 2017; Hanke *et al.*, 2017; Yoda *et al.*, 2018). Hanke *et al.* (2017) showed that a nonzero static orbital moment can arise in the noncoplanar antiferromagnet γ-FeMn without SOC due to spin chirality. Here, in the absence of spin chirality, we predict nonzero orbital moments that are present without SOC but permitted by $\mathcal{PT}$ symmetry when an applied electric field is present. Yoda *et al.* (2018) proposed that in a chiral crystal the solenoidal electron hopping motion could lead to an orbital magnetization in systems with time-reversal symmetry, in the sense of an orbital Edelstein effect. Our here-computed induced orbital polarization is distinctly different, as it does not require chiral crystal symmetry.

2. Frequency and magnetization dependence

Our calculations predict sizable induced polarizations at finite frequencies, which raises the question whether electric field driven magnetic moment switching could be achieved at high frequencies. It is well known that time-dependent magnetic fields cannot drive fast spin dynamics of ferromagnets in the optical regime because the magnetic permeability $\mu(\omega)$ decays quickly as ω increases to the infrared region (Kittel, 1946). The situation is however entirely different for the SREE and OREE. The magnetic permeability is due to a magnetic field $\boldsymbol{H}$ that acts on the spin through the Zeeman interaction in the Hamiltonian, $\mu_{\mathrm{B}}\,\hat{\boldsymbol{\sigma}} \cdot \boldsymbol{H}(t)$, whereas for the SREE the electric field couples to the charge, $-e\hat{\boldsymbol{r}} \cdot \boldsymbol{E}(t)$. The electric charges can indeed follow the rapidly changing E-field, implying that an equally fast magnetic response can be anticipated. Due to their electrical origin,

the induced magnetizations can be driven at petahertz frequencies, thus opening for potential routes to achieve petahertz spintronics. This would be so particularly for thin functional devices, since the penetration depth of optical fields is typically $\leq 20\,\mathrm{nm}$.

In the DC limit, $\omega = 0$, the real part of the REE is nonzero and its imaginary part vanishes exactly. At finite frequencies, both the real and imaginary parts of the tensor components can be nonzero. The nonzero imaginary REE susceptibility has a specific influence on the evolving magnetization dynamics. For a given driving electric field $\boldsymbol{E}(t)$, the induced spin polarization $\delta \boldsymbol{M}^S(t)$ can be retrieved from a Fourier transform of $\delta \boldsymbol{M}^S(\omega) = \chi^S(\omega)\boldsymbol{E}(\omega)$. The induced spin polarization follows the driving field, but it has a phase difference due to the imaginary SREE susceptibility. An equivalent relation holds for the orbital polarization. The induced spin and orbital polarizations at a frequency ω will thus still provide staggered torques on the existing static moments, but these torques will alternate with time. A major question is then how fast the switching of the static moments can proceed, whether this can be pushed to the PHz regime. Recent experiments demonstrated that switching of CuMnAs is possible at THz frequencies (Olejník *et al.*, 2018). Potentially, on account of the above, the switching could thus be even faster in antiferromagnets, in particular when the torques could be enhanced, but the boundaries on the switching speed are as yet unexplored.

To verify whether the SREE and/or OREE can be at the origin of ultrafast switching, and what the intrinsic frequency limit is, atomistic spin-dynamics simulations should be performed. The inclusion of both induced spin and orbital magnetic moments would notably be required to achieve the full picture. Such spin-dynamics simulations could clarify as well the role of the non-staggered, homogeneous components for the switching and the influence of Joule heating, inherently present in all experiments. It was shown recently that Joule heating plays an essential role as it drastically decreases the required switching field and enhances the spin-orbit torque efficiency (Li *et al.*, 2018). Also for $\mathrm{Mn_2Au}$ it was lately concluded that Joule heating can provide a sufficient thermal activation for switching processes (Meinert *et al.*, 2018). It should be emphasized, too, that the switching dynamics of an antiferromagnet is distinct from that of a ferromagnet, since the magnetization dynamics of an antiferromagnet is described by a second-order differential equation, which contains a magnetic inertia term for the spins (Kim *et al.*, 2017; Kimel *et al.*, 2009; Mondal *et al.*, 2017). Antiferromagnetic inertia can provide an important stimulus for the switching, because, even after the pulse is switched off, the already induced torques will act for a longer time as drivers of the dynamics.

D. Concluding remarks on REE of Mn₂Au and CuMnAs

Switching in AFMs is believed to be due to locally staggered spin-orbit fields that drive opposite dynamics of moments on the two AFM sublattices (Bodnar *et al.*, 2018; Godinho *et al.*, 2018; Grzybowski *et al.*, 2017; Meinert *et al.*, 2018; Olejník *et al.*, 2017, 2018; Wadley *et al.*, 2016; Železný *et al.*, 2014). Our investigation strongly supports that the REE is an excellent candidate to explain the microscopic origin of such staggered fields. Beyond this, we report several surprising discoveries: first, there exists a significant orbital REE that can be much larger than the spin REE. Second, we find that there exists not only staggered but also non-staggered components to the REE tensors. In both CuMnAs and $\mathrm{Mn_2Au}$, we find that the staggered response is strongest. This causes a locking of the orbital momentum perpendicular to the applied field.

Computing the symmetry of the induced polarizations with respect to an in-plane electric field, we find that these can have a Rashba-like or a Dresselhaus-like texture and that these textures can in general be distinct for the induced spin and orbital polarizations; for example, a Dresselhaus-like symmetry for the SREE and a Rashba symmetry for the OREE of $\mathrm{Mn_2Au}$ with in-plane AFM moments. As a consequence, the spin and orbital fields can enhance each other or cancel each other, i.e., act in a cooperative or a non-cooperative way for switching of the sublattice magnetizations.

The most surprising part of this work is undoubtedly the strong induced orbital polarization, which can be much larger than the induced spin dipole magnetization. The nonequilibrium orbital magnetization is notably even present in the absence of spin-orbit interaction. This implies that it does not arise from a small relativistic effect, but has a more fundamental, nonrelativistic origin, allowed by the $\mathcal{PT}$ symmetry of the two Mn inversion partners. While our focus here has been on the two AFMs that are of current interest for antiferromagnetic spintronics, the large dominant orbital fields could gain importance in the emerging field of spinorbitronics (Manchon and Belabbes, 2017). As the induced spin and orbital polarizations originate from the coupling of the electric field to the electron charges, these induced polarizations can moreover be driven at high frequencies, opening prospects for achieving spintronics at petahertz frequencies.

Lastly, on a more general note, the here-developed general ab initio framework can be employed for the study of nonequilibrium electric-field induced polarizations in a wide range of materials, as e.g. bulk compounds and metal/ferromagnet or metal/antiferromagnet interfaces. While bulk materials can already display rich spin-orbit-related physics, interfaces of a heavy metal with a magnetic layer, where the SOC is increased at the interface, can feature an enhanced Rashba-Edelstein effect that can

e.g. be utilized to control the spin orientation in the magnetic layer (Manchon *et al.*, 2015). The developed *ab initio* framework can provide a materials' specific understanding of the mechanisms behind electrical spin control and lead to the design of suitable interfaces for future spintronics applications.

III. MODELLING OF THZ SPECTRA: FROM DIFFUSION TO SUPERDIFFUSION

A. Spin-charge interconversion and THz spectra from spin-polarized hot electrons: a simple diffusive approach

The specific impact of an exciting pulsed laser mode on a material requires some adequate modelling of the ensuing spin transport and spin relaxation. The two-temperature model describing the electronic absorption and giving rise to electronic heating with characteristic excitation energy over the Fermi level (temperature T_e followed by inelastic relaxation due to electron-electron interactions and phonon bath characterized by a second temperature T_{ph} (Maldonado *et al.*, 2017) is well adapted for this purpose. A refined modelling generally requires a *superdiffusive* approach for the excited carriers that will be described further below. Note that in this scenario, the fast electron energy and spin relaxation rate in the heavy transition metals and related alloys (Pt, Au:W, Au:Ta) investigated here makes that the two different temperature dynamics becomes more and more uncoupled, leading to solely the electron dynamics becoming relevant for the THz emission spectra.

One goal of the present work is to highlight the major role of the electronic properties of the materials constituting the spintronic THz emitters in order to optimize these systems in terms of emission efficiency. The simpler analysis presented in this Section addresses then *i*) the time-dependent diffusion and relaxation processes in separate layers of excited spin-polarized carriers, generated by a short laser pulse and characterized by a certain generation rate $\mathcal{P}(\mathbf{r},t)$; *ii*) the reflection/transmission of the spin-polarized hot carriers at the inner interface, as well as *iii*) the specific boundary conditions to consider at the two outward interfaces. Regarding point *ii*), the transmission across the inner interface can involve spin-mixing terms. *In fine*, the impact of the mobility of electrons and/or the material's resistivity will be put forward through our simulations and compared to our experimental data obtained in WP1.

The present work and contribution described in detail below has given rise to the publication of a paper that appeared recently in the Applied Physics Review journal (Dang *et al.*, 2020) within the S-Nebula framework.

1. Boltzmann formalism

The description of the time-domain dynamics of hot-electrons within spintronic multilayers excited by ultra-short laser pulses may be performed in the frame of the Boltzmann transport theory and equations (BTE), and considering the different electronic diffusion and relaxation processes. The BTE for spin-polarized particles can be derived as the evolution equation for a reduced single-particle density matrix. It also accounts for the properties of excited electron dynamics in the *sp* bands of very thin metal layers, as widely discussed in the superdiffusive theory of spin currents in both experiments and in modelling (Battiato *et al.*, 2010, 2012; Lu *et al.*, 2020; Maldonado *et al.*, 2017). We start from the evolution equation for the carrier-distribution function in the following form:

$$\left[\frac{\partial}{\partial t} + \frac{\hbar}{m^*}\mathbf{k}\cdot\nabla_{\mathbf{r}} + \frac{1}{\hbar}\mathbf{E}_\sigma(\mathbf{r},t)\cdot\nabla_{\mathbf{k}}\right]f_\sigma(\mathbf{r},\mathbf{k},t)$$
$$= \mathcal{P}_\sigma(\mathbf{r},\mathbf{k},t) - \frac{f_\sigma(\mathbf{r},\mathbf{k},t)}{\tau_\sigma(\mathbf{r},E)}$$
$$+ \sum_{\sigma,\sigma'}\int d^3k'\ w(\mathbf{r};k',\sigma';\mathbf{k})f_\sigma(\mathbf{r},k',t)\ , \qquad (26)$$

where f_σ represents the spin- and time-dependent distribution function in space ($\mathbf{r}$) and in the reciprocal space or Brillouin zone ($\mathbf{k}$), $\mathbf{E}$ the electric field, and where $\mathcal{P}_\sigma(\mathbf{r},\mathbf{k},t)$ is the pump term due to the pulsed laser excitation. In general, the distribution function $f_\sigma = f_\sigma^0 + \phi_\sigma$ can be separated into a sum of an equilibrium part $f_\sigma^0(E)$ plus a non-equilibrium (thermal) part $\phi_\sigma(\mathbf{r},\mathbf{k},t)$ describing thus the electronic excitations (ϕ_σ is called g_σ by Valet and Fert (1993)). The two relaxation terms at the right hand side of Eq. (26) represent the respective *scattering-out* and *scattering-in* processes in the BTE. We particularly focus here on the Co(2nm)/Pt(4nm) system giving convincing quantitative THz results. The dynamics of the system is performed using the BTE involving the time dynamics of both spin-dependent carrier densities and spin-currents by using a Finite Difference time domain treatment (FDTD).

B. *Ab initio* calculations of transparencies at Co/Pt interfaces

First-principles calculations giving the energy-dependence of the electronic transmission coefficient for the Co/Pt(111) interface were performed within the atomic sphere approximation in the Green's function-based tight-binding linear muffin-tin orbital (GF-LMTO) method (Gunnarsson *et al.*, 1983; Pashov *et al.*, 2019; Turek *et al.*, 1997), treating exchange and correlation within the local-density approximation (LDA) (von Barth and Hedin, 1972). The Green's functions are represented in a mixed basis: the two-dimensional translational periodicity of the interface allows one to introduce the conserved wave vector component
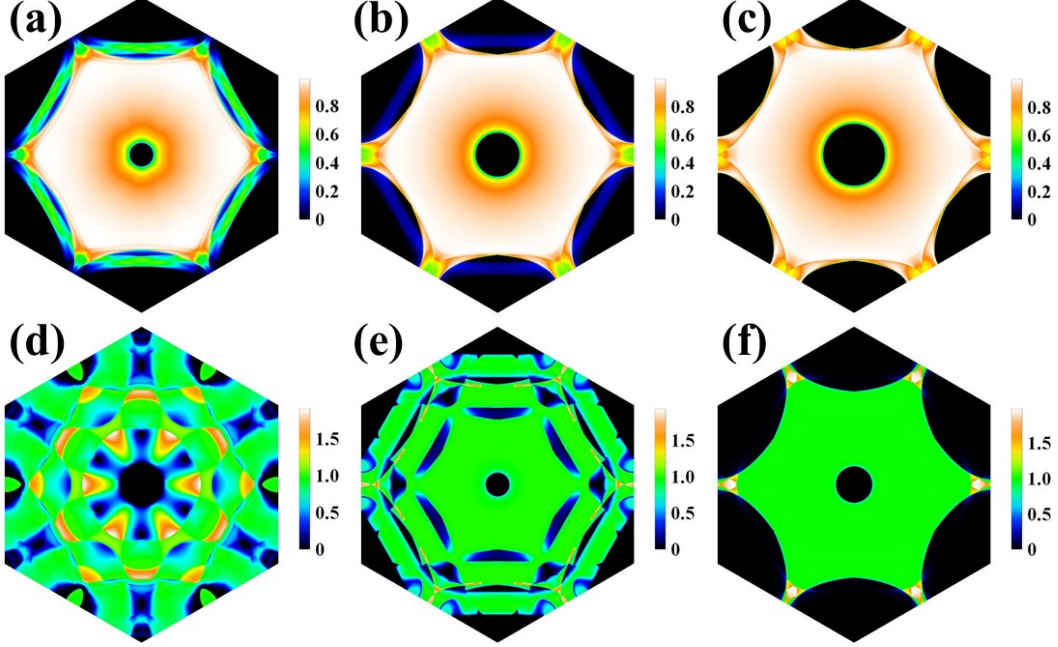
FIG. 14 Calculated energy-dependent and selected-spin transmission function for the Co/Pt (111) interface plotted as a function of $k_\parallel$ (projection of the wave vector on the plane of the interface, which is conserved in the scattering process) and summed in the two-dimensional Brillouin zone of the interface. (a-c): Majority-spin, (d-f): minority-spin channel. Panels (a) and (d): $E - E_F = 0$, (b) and (e): 0.5 eV, (c) and (f): 1.0 eV. Those calculations shows that near the Fermi level (a-d), the majority electrons (spins $\uparrow$) are more easily transmitted (in average) than the minority spin channel ($\downarrow$), in particular near the Brillouin zone center, whereas at higher energy, 0.5 eV above the Fermi level (e-f), the electronic transmission for the minority spin channel is larger (refer to Fig. 15).

$k_\parallel$ parallel to the interface, which is confined to the two-dimensional Brillouin zone of the interface; the Green's function is then a matrix in real space with arguments confined to the unit cell of the 'active region' including the interface and a few monolayers on each side of it. The active region is embedded between semi-infinite Co and Pt leads. After the self-consistent charge and spin densities were obtained, the total and $k_\parallel$-resolved energy-dependent ballistic conductance of the Co/Pt bilayer was calculated using the Landauer-Büttiker technique. We assumed the Co/Pt bilayer has a perfect continuous face-centered cubic lattice with an abrupt (111) interface and a common lattice parameter of 2.64 Å, ignoring strain relaxation. The average transmission probability for electrons incident from the Co side is:

$$\bar{T}_\sigma^{\mathrm{Co}\to\mathrm{Pt}} = \frac{1}{N_\sigma^{\mathrm{Co}}} \sum_n T_\sigma^n = \frac{g_\sigma}{g_\sigma^{\mathrm{Co}}}, \qquad (27)$$

where σ denotes the spin channel, N_σ^{Co} is the number of conducting channels of a given spin in the Co lead, T_σ^n the transmission probability for one of these channels n,

g_σ the conductance of the Co/Pt bilayer, and g_σ^{Co} the Sharvin conductance of the Co lead.

Cobalt has one majority-spin Fermi-surface sheet with topology identical to that of Cu: the somewhat distorted free-electron-like Fermi surface does not quite fit into the first Brillouin zone, forming 'necks' centered around the L points on its hexagonal faces. One of these L points projects onto the center ($\bar{\Gamma}$ point) of the surface Brillouin zone of the (111) interface, resulting in a circular "hole" in the transmission function [panels (a-c) of Fig. 14] where there are no bulk states in Co. As the energy increases, the iso-energetic surface expands, and the holes become larger. Panels (a-c) in Fig. 14 show that most the states from the majority-spin Fermi surface sheet in Co have a high probability of transmission across the interface in the entire energy window shown in Fig. 15(a). This feature is similar to the well-known case of the Co/Cu interface (Schep *et al.*, 1997) where the band structure match in the majority-spin channel is nearly perfect.

Because Pt has one electron fewer than Cu and open $5d$ shells, its Fermi surface is more complicated, with one free-electron-like electronic sheet, one extended hole-like
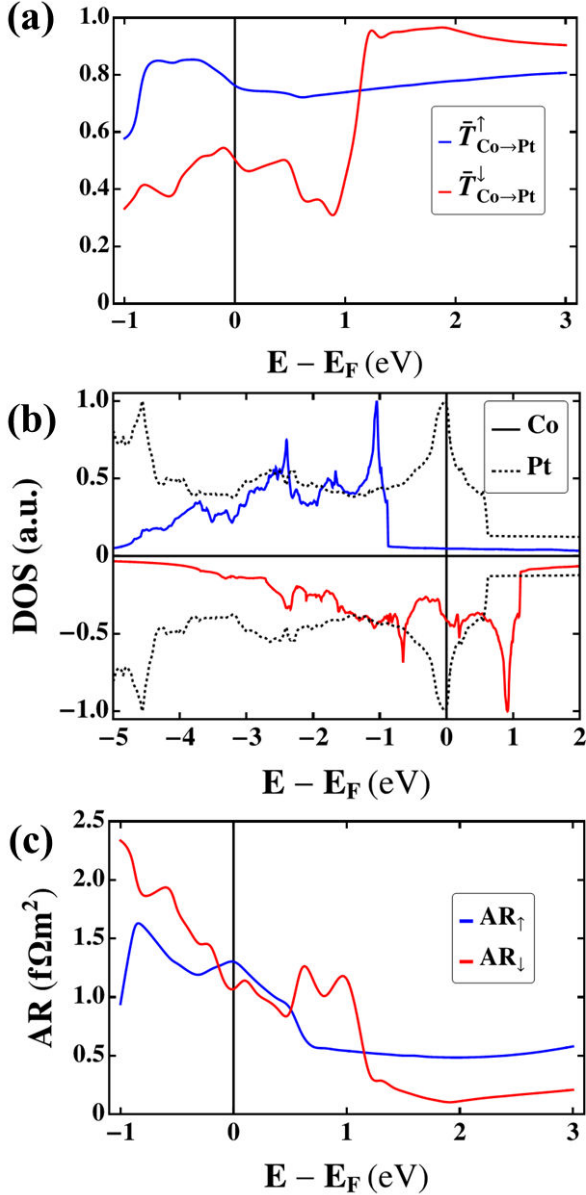
FIG. 15 (a) Spin and energy-dependent average transmission probability for electrons incident from the Co side on the Co/Pt (111) interface, see Eq. (27). Blue (red) lines: majority (minority) spin electrons. (b) Density of states in bulk fcc Co and Pt with the lattice parameter used in the calculations for the interface. Blue (red) solid lines: majority-spin (minority-spin) electrons in fcc Co. Dotted lines: both spins in Pt. (c) Effective spin- and energy-dependent area-resistance product of the Co/Pt (111) interface. Blue (red) line: majority (minority) spin.

sheet that projects to the periphery of the (111) surface Brillouin zone, and one small hole-like pocket around the X point. As the energy is increased, the hole-like sheets shrink and disappear at about 0.7 eV where DOS has a van Hove singularity (see Fig. 15(b)). The majority-spin

transmission $\bar{T}_{\uparrow}^{\mathrm{Co} \to \mathrm{Pt}}$ is essentially unaffected by the disappearance of the hole-like sheets in Pt, because, as is clear from Fig. 14(a-c), the majority-spin transmission is dominated by electrons from Co transmitting into the electron-like sheet in Pt. On the other hand, $\bar{T}_{\downarrow}^{\mathrm{Co} \to \mathrm{Pt}}$ decreases significantly in the $0.5 - 0.7$ eV range and remains suppressed up to about 1.0 eV, where it quickly rises up to almost 1. The drop around 0.6 eV is associated with the closure of the hole-like sheet in Pt, which decreases the transmission probability of the minority-spin states from Co. The rise at $1.0 - 1.2$ eV is due to the closure of the similar hole-like minority-spin sheets in Co, the electrons from which transmit poorly into Pt but contribute significantly to the Sharvin conductance of Co.

Fig. 15(a) shows that the Co/Pt (111) interface has this favorable property in the energy window from 0 to 1.0 eV above the Fermi level, and especially in the $0.6 - 1.0$ eV range, between the top of the $5d$ band of Pt and the top of the minority-spin $3d$ band of Co. Fig. 15(c) also shows the spin-resolved effective interfacial area-resistance product calculated according to Schep *et al.* (1997) This quantity represents the apparent spin-dependent resistance of the interface in the circuit under diffusive transport conditions. Although these conditions are not satisfied in THz emission devices, and transport of hot electrons brings its own complications, the spin-dependent effective RA product can serve as an approximate indicator of the interfacial spin asymmetry (noted as the γ parameter). Here we also see that the Co/Pt (111) interface has a larger effective resistance in the minority-spin channel for energies in the $0.6 - 1.1$ eV range that is in the energy region of hot electrons generated by pulsed laser excitations, suggesting an additional 'spin-filtering' effect and an enhancement of the spin current by this interface.

1. FDTD simulations in the time domain

Solving the time-dependent equations requires the implementation of a numerical routine. The experimental boundary conditions corresponding to pulse laser excitation is considered by a zero σ-spin population within the whole multilayers at $t = 0$. Additional treatment of the external and internal boundary conditions is available in the following reference. We have considered a typical temporal Gaussian shape:

$$\mathcal{P}_{\sigma}^{0}(\mathbf{r}, t) = \mathcal{P}_{\sigma}^{0}(t) = s_{\sigma} \frac{A}{\sqrt{2\pi\Delta t^2}} \exp\left[-\frac{(t - 4\Delta t)^2}{2\Delta t^2}\right], \quad (28)$$

uniformly exciting the ferromagnetic material with a wavelength $\lambda \simeq 810$ nm. A is related to the laser pump power, Δt the laser pulse duration (typically 100 fs) and s_{σ} the initial proportion of the spin-channel excited owing to the different density of states $\mathcal{N}_{d,\sigma}$ of the d-band.
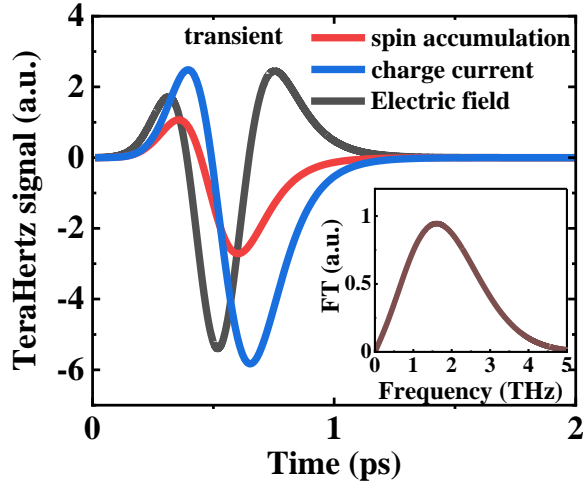
FIG. 16 Typical simulated time-domain evolution of the emitted electric field terahertz signal (grey) calculated for a Co(2)/Pt(4) structure excited by a 100 fs laser pulse in Co. The generated transient ultrafast surface charge current j_c (blue) and out-of-equilibrium spin accumulation (m) (red) are plotted at the interface $z = 0+$ on the Pt side. The Fourier transform (FT) of the corresponding terahertz signal is given in the inset. The typical slope of the FT signal at low frequency is representative of a derivative signal ($E_{THz} \propto \frac{\partial J_c}{\partial t}$). In those simulations, inner average transmission coefficient is $T^\star = 0.2$ and the spin interfacial asymmetry was fixed to $\gamma = 0.5$.

Our numerical investigations mainly focused on the major role played in the terahertz wave generation by interfacial transmission T_σ calculated by *ab initio* and described the shape of the typical THz spectra. We considered the change in the spectra obtained by varying, in the same way, both the momentum relaxation time τ_p and the spin-flip time τ_{sf} from their nominal values τ_p^0 and τ_{sf}^0. We consider the scaling parameter:

$$\alpha = \frac{\tau_{sf}}{\tau_{sf}^0} = \frac{\tau_p}{\tau_p^0} \qquad (29)$$

in the ferromagnet (FM) and in the heavy metal (HM) allowing to simulate the effect of a mobility change of the different constituents (Pt *vs.* Au-based alloys), keeping fixed their spin-orbit parameter. We have previously checked that our simulations give the correct conclusions in the steady-state regime of spin-injection (CW pump).

In order to first explore the strong impact of the transmission T_σ and the observed differences between the Co/Pt and transition metal alloys (WP1), we considered the spin average transmission $T^\star$ and spin-asymmetry γ, as extracted from the *ab initio* calculations:

$$T_\sigma = \frac{T^\star}{1 \mp \gamma} \quad \Rightarrow \quad T^\star = \frac{1 - \gamma^2}{2} \left(T_\uparrow + T_\downarrow \right), \qquad (30)$$

with $T^\star = 0.2$ and $\gamma = +0.5$ at ϵ_F (Fig. 15). We extracted

the typical dependence of (Fig. 16):

i) the out-of-equilibrium spin accumulation or spin-density profile within the multilayer,

ii) the corresponding profile of the ultrafast charge current within the muitilayer.

iii) the electrical profile of the THz electric field (E_{THz}) in the time domain and in the far-field region in close agreement to both Co(2)/Pt(4) and NiFe(2)/Pt(4) data in shape.

Regarding the spectral representation of the signal in the frequency domain, it covers a wide and continuous band up to 5 THz, and fits reasonably well in form with our experimental data, taking into account the spectral bandwidth limitation of our detector.

2. FDTD simulations in the frequency domain

a. *Impact of the electronic transmission.*

We have also investigated the influence of the inner transmission coefficient $T^\star$ at the FM/HM interface. A relevant information is the intensity ratio between subsequent THz spectra *vs.* $T^\star$. For increasing $T^\star$ from 10^{-4} to 0.5, the spectra increases in amplitude by about the same proportion. The terahertz signal is the largest for $T^\star = 0.5$ for both pump polarization that is for either minority (Fig. 17(a)) and majority pumped spins (Fig. 17(b)). Alongside the difference in their conductivity and in their spin-diffusion length, T^* mainly explains the strong difference in the THz spectra between Co/Pt, NiFe/Pt on one side and THz spectra from alloys (Au:W or Au:Ta) on the other hand when the transmission for the latter decreases by roughly one order of magnitude.

b. *Effect of material conductivity and spin-flip rate on the THz spectra.*

We have moreover explored the effect on the THz spectra of the spin-flip rate in both HM and FM that may be probed in future experiments. One considers here the case of favorably minority spin pumped, $s_\uparrow = 0.5$ and $s_\downarrow = 1$ and spin-filtering of majority electrons ($\gamma = +0.5$). The typical evolution of THz-TDS spectra resulting from a pump pulse of 100 fs on varying $\alpha = 0.1, 0.3, 1, 3, 10$ in FM and HM are reported on respective Figs. 18(a-b)) and Figs. 18(c-d)) for $T^\star = 10^{-1}$ (Figs. 18(a-c)) and $T^\star = 10^{-3}$ (Figs. 18(b-d)). Two major conclusions can be drawn:

- Concerning the dependence on α_{FM}, and for $T^* = 0.1$ (Fig. 18(a)), one notes a significant increase of the THz signal while increasing α_{FM} from 0.1 to 10.

- On the other hand, increasing the α_{HM} ratio increases the amplitude of the THz spectra (Fig. 18(c-d)) owing to a higher mobility, leading to a larger spin-diffusion length and larger volume of charge relaxation in HM. In this sense we demonstrate here the relationship
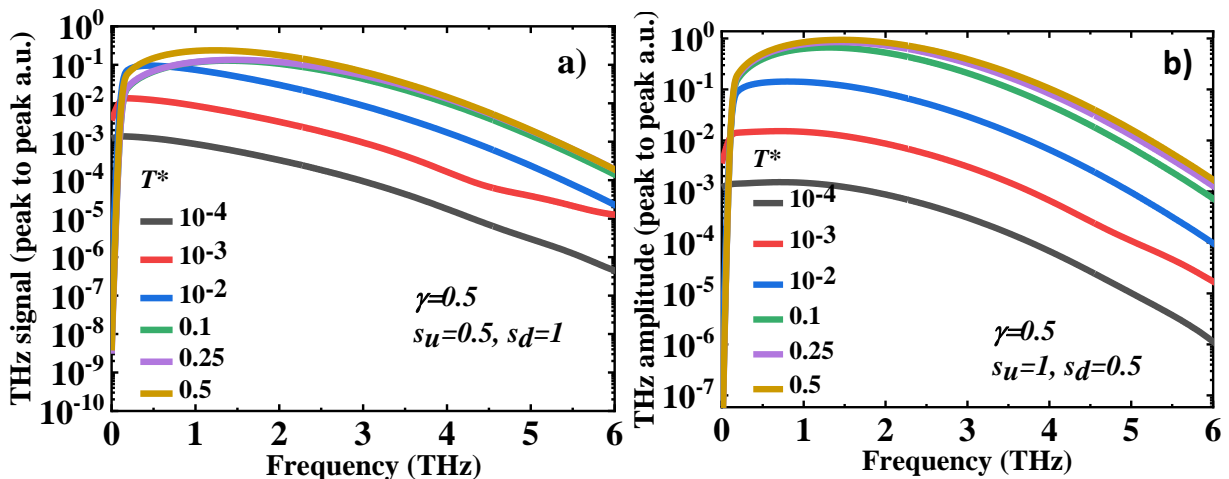
FIG. 17 Simulation results showing the frequency-domain representation (Fourier transform: FT) of the emitted terahertz electric field spectra E_{THz} (in log. scale) in the case of Co(2)/Pt(4) excited by a short 100 fs laser pulse and calculated for different average transmission coefficient from $T^* = 10^{-4}$ to $T = 0.5$. The initial spin polarisation was reversed from (a) $s_\uparrow = 0.5$, $s_\downarrow = 1$ to (b) $s_\uparrow = 1$, $s_\downarrow = 0.5$ (b) while keeping fixed the interfacial spin-asymmetry coefficient $\gamma = +0.5$ through all the simulations. These simulations emphasize the particular role of the so-called interfacial 'spin-filtering' effect played by interfaces on the THz spectra.

by which E_{THz} follows the local HM conductivity (or HM mobility) in proportion to α_{HM}. This feature is clearly demonstrated in Fig. 18(c-d) whatever $T^\star$ is and also evidenced experimentally when comparing (Co,NiFe)/Pt and NiFe/Au based alloys. Note that the change of α_{HM} does not imply a variation of the spin-orbit parameter (ϵ_{HM}) avoiding thus the possible effect of the so-called impedance mismatch between FM and HM.

C. The superdiffusive model

The superdiffusive model provides a more elaborate and more precise description of the spin transport of hot, laser-excited electrons in a metallic heterostructure (Battiato *et al.*, 2010, 2012; Eschenlohr *et al.*, 2013; Hofherr *et al.*, 2017; Rudolf *et al.*, 2012). In contrast to the more simplified diffusive approach given above, the superdiffusive model is based, first, on excitation of different amounts of spin-majority and spin-minority electrons through the ultrashort laser pulse. The excited spin-polarized hot electrons will initially move isotropically through the material. In this initial stage, the propagation of each hot electron is ballistic. Second, depending on their spin lifetime, the spin-majority and minority electrons undergo scattering events through which they loose energy and at the same time excite secondary hot electrons. Note that the scattering lifetime of a hot electron in Pt is of the order of 15 fs (Freeman *et al.*, 2018). Through these scattering events, the hot electrons begin to thermalize with other, cold electrons. After a few scatterings the transport of the hot electrons has become superdiffusive (which is characterized by the so-

called anomalous diffusion coefficient d_w, being between 1 (i.e., ballistic) and 2 (i.e., diffusive) (Battiato *et al.*, 2012)). Third, the hot spin-polarized electrons thermalize further when they undergo more scatterings. After about 500 fs they have lost their excess energy and the laser-induced transport approaches the diffusive regime (Battiato *et al.*, 2012).

Before giving a mathematical formulation, it is instructive to understand how superdiffusive transport leads to a nonequilibrium spin current in a FM that is subsequently injected into a HM layer, where it is converted by the inverse SHE and causes THz dipole emission (Kampfrath *et al.*, 2013). The velocities of the hot spin-polarized electrons v_σ as well as their spin lifetimes, τ_σ are strongly spin dependent in the common FMs Fe, Co, and Ni. Previous *ab initio* calculations have provided values for these quantities (Zhukov *et al.*, 2005, 2006). The spin lifetime and velocities of the spin-majority electrons is larger (sometimes much larger) than the corresponding quantities of the spin-minority electrons. As a result, the spin-minority electrons will scatter more and loose energy faster than the majority-spin electrons. The latter will propagate faster away from the excited layer and form so a spin-polarized current that can quickly enter an adjacent HM metal layer. Due to dielectric screening in the metal the spin-polarized current will be to a good approximation be a spin current. Experiments on 10-nm Ni/150-nm Au bilayers have shown that the spin current from the laser-excited Ni film enters the Au film in about 40 fs (Hofherr *et al.*, 2017). This process is material's dependent, thickness dependent, and also the spin transparency of the interface, see Sec. III B, plays a role. For a recent experimental overview,
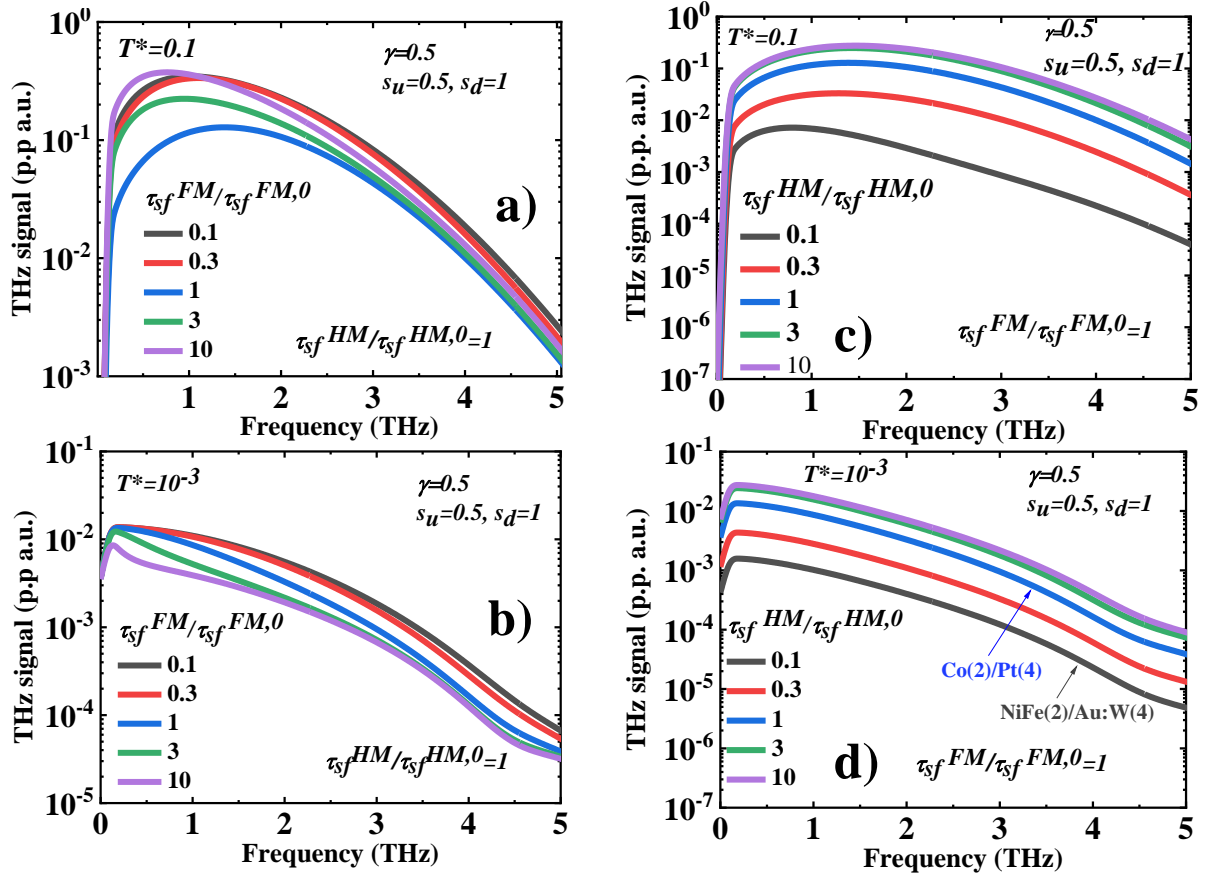
FIG. 18 Frequency-domain (FT) representation of the emitted electric field (E_{THz}) terahertz spectra obtained for Co(2)/Pt(4) after a short 100 fs 810 nm laser pulse and considering an initial spin polarisation $s_\uparrow = 0.5$, $s_\downarrow = 1$. The study focuses on the major role played by the spin dynamics timescale change for a fixed transmission parameter respectively equal to (i) $T^\star = 10^{-1}$ (a and c) and (ii) $T^\star = 10^{-3}$ (b and d). Those calculations were performed with respect to the transformation Eq. (29) for the ferromagnetic layer characterized by a spin scattering time τ_{sf}^{FM} (a and b) and for the heavy metal characterized by a spin scattering time τ_{sf}^{HM} (c and d). The transformation coefficient α is swept in the $[0.1 - 10]$ range. A constant $\gamma = +0.5$ value was kept for the whole simulations.

see Malinowski *et al.* (2018).

To model the spin transport in the superdiffusive region a hybrid approach can be used. This consists of classical kinematic modeling of the hot electron as a particle that scatters repeatedly and so propagates while loosing energy. The quantum information that is embedded in the spin is however kept, giving each particle a spin-dependent velocity and spin-lifetime. This approximation is justified by the fact that the scattering lifetime of a hot electron in a typical metal can be of the order of 10 fs, but its spin life is much longer typically 250 fs (see e.g. Carva *et al.* (2013)). Hence, to a first approximation the hot electron undergoes spin-conserving scattering events.

In the superdiffusion model, one keeps mathematically track of the hot spin-polarized electrons by counting the number of scattering events. This makes the model computationally more demanding than the simpler diffusive model. A longer derivation (Battiato *et al.*, 2010, 2012)

leads to the transport equation for the full (spin) density $n(\sigma, E, z, t)$

$$\frac{\partial n}{\partial t} + \frac{n}{\tau} = \left(-\frac{\partial}{\partial z} \hat{\phi} + \hat{I} \right) \left(\hat{S} n + S^{ext} \right), \qquad (31)$$

where $\hat{I}$ is the identity operator and $n = \sum_{N=1,\infty} n^{[N]}$, with $n^{[N]}$ the particle density after $N-1$ scattering events; all scattering events are summed. E is the energy of the hot electron above the Fermi energy. Note that $\tau = \tau(\sigma, E, z)$, i.e., it depends on the spin and energy of the hot electron. z represents the spacial coordinate along the normal to the metallic film. Thus, τ changes when the hot electron crosses an interface between two metal layers. $\hat{\phi}$ is the flux of spin-dependent hot electrons which depends on the electron velocities, see Battiato *et al.* (2012). S^{ext} is the source term, i.e., the hot spin-polarized electrons generated by the laser pulse.

Using the assumption that incoming and out-going directions of scattering electrons are uncorrelated, the particle after being scattered behaves actually as if being excited by an effective source

$$\hat{S}n = \sum_{\sigma'} \int p\left(\sigma, \sigma', E, E', z\right) \frac{n\left(\sigma', E', z, t\right)}{\tau\left(\sigma', E', z\right)} dE', \quad (32)$$

which is the scattering term at all energies weighted by the transition probability after a scattering, $p(\sigma, \sigma', E, E', z)$. This quantity treats inelastic and elastic scattering events and electron cascades. In this still general expression it contains the spin-conserving scattering probability and can include the probability for spin-flip scattering as well. Since Eq. (31) has to be satisfied for every value of σ and E, we effectively have a set of coupled equations that has to be solved. As a result, the simulations require substantial computer time. A faster way to compute the spin current could be the recently proposed particle-in-cell approach (Nenno *et al.*, 2018). The simulations of the superdiffusive spin currents have been employed recently by us to study the problem of laser-induced domain-wall motion. The superdiffusive spin currents can generate a very fast domain wall motion of 10^4 m/s (Baláž *et al.*, 2020). Also, as we showed recently the superdiffusive spin currents generated in a ferromagnetic layer can excite THz spin waves in another ferromagnetic layer in trilayer structures (Ritzmann *et al.*, 2020).

IV. ELECTRONIC PROPERTIES OF BI-BASED RASHBA AND TOPOLOGICAL INTERFACES

A. Bi$_{1-x}$Sb$_x$ (BiSb) topological insulators and Co/BiSb bilayers and spin-charge interconversion for THz emission

This work and contribution deals with the calculation of the electronic properties of surface states of Bi$_{1-x}$Sb$_x$ compound known to be a topological insulator material. This is strongly related to the demonstration of THz results obtained on Co(4nm)/Bi$_{1-x}$Sb$_x$(30, 15, 5, 2.5nm) with $x = 0.1, 0.15, 0.2, 0.3, 0.4$ the content of the Sb atomic species.

There is today a considerable interest in the fundamentals and electronic properties of the (111) surface of Bi and Bi$_{1-x}$Sb$_x$ related materials owing to their specific properties to exhibit topological spin-textured surfaces states in their gap (Benia *et al.*, 2015; Hsieh *et al.*, 2008). The interest would be then to promote efficient spin-charge interconversion (Chi *et al.*, 2020) for enhanced THz emission owing to the inverse Rashba-Edelstein effect (IEE). In those systems, the BiSb(111) surface is composed of hexagonal atomic layers stacked along the [111] direction with two alternating interlayer spacings (see Fig. (19)). A pair of nearest-neighbor layers with

shorter layer spacing, which forms a two-dimensional (2D) buckled honeycomb lattice, is covalently bonded, while the bonding between neighboring bilayers with larger interlayer spacing is weaker (Liu and Allen, 1995). The surface band structure of clean Bi(111) and that of alloyed Bi$_{1-x}$Sb$_x$ compounds have also been a subject of extensive studies. While the valence bands of a three-dimensional (3D) Bi crystal is topologically trivial in contrast to those of Sb, two spin-polarized surface bands appear in the projected bulk band gap of Bi(111). They exhibit a large Rashba-type spin splitting due to large spin–orbit interactions among the Bi $5p$ orbital components. These two bands should form a degenerate Kramers pair at the two time-reversal invariant momentum (TRIM) points, $\overline{\Gamma}$ and $\overline{M}$, in the hexagonal surface Brillouin zone (SBZ) (Ishida, 2016; Teo *et al.*, 2008). However, the DFT calculation of Koroteev *et al.* (2008) revealed that when the surface is represented by a slab model, the two surface bands at the $\overline{M}$ point exhibit a sizable energy splitting due to the interaction of the two surfaces of the slab even for a relatively thick slab. Moreover, some recent results indicate that the electron wave function of the surface bands on Bi(111) decays quite slowly toward the interior of the crystal around the $\overline{M}$ point. This was recently demonstrated by photoemission electron spectroscopy (Benia *et al.*, 2015).

Surface states of materials with strong spin-orbit interactions reveal very interesting options to achieve charge and spin transport through surface states as well as spin-charge interconversion (Chi *et al.*, 2020). The spatial extent of the surface-state wave functions in the surface normal direction should be an important parameter in determining their scattering rate into bulk states, as well as the distortion of such states by contact with the ferromagnetic transition metal (Co). The purpose of these calculation is to explore the decay depth of the surface-state wave functions of Bi(111) as a function of 2D wave vector k. Also, we wish to calculate the spin-charge interconversion in contact with Co and deconvolve the respective surface and bulk contributions through thickness dependence of the signal (from both experimental and theoretical point of view).

Although first-principles band calculations have already revealed the Fermi surface and the energy band structure (Ishida, 2016), no systematic analysis of the spin-texture properties and spin-charge interconversion power for comparison with the reported angular-resolved photoemission spectroscopy (ARPES) method and results has been performed, in particular when a ferromagnetic layer is set on the top. Here, we approach this issue using an sp_3 basis. For this purpose, we calculate the electronic structure of Co/BiSb systems by tight-binding methods (TB) in both bulk and slab structures, and using various parametrizations (Liu and Allen, 1995; Ohtsubo and Kimura, 2016; Saito *et al.*, 2016; Teo *et al.*, 2008). Bi possesses a rhombohedral Bravais lattice with two atoms
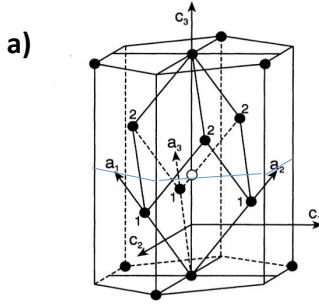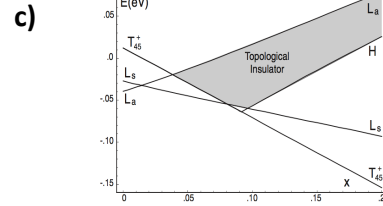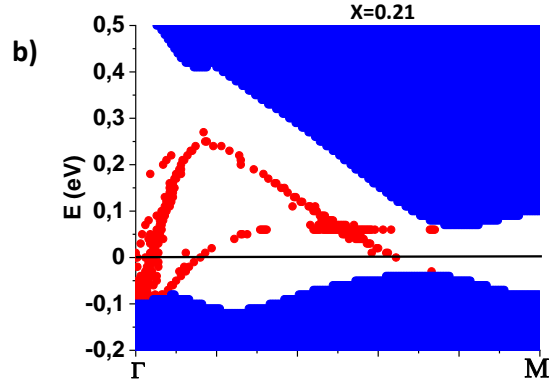
a)

FIG. 1. Crystal structure of Sb and Bi, showing first and second neighbors (labeled 1 and 2) to the central atom represented by an open circle. The bisectrix (C_1), binary (C_2) and trigonal (C_3) axes, and primitive translation vectors (a_1, a_2, a_3) are also shown.

The hopping parameters for Bi$_{1-x}$Sb$_x$:

$$V_c(x) = x V_c^{Sb} + (1 - x^2) V_c^{Bi}.$$

*Jeffrey C. Y. Teo, Liang Fu, and C. L. Kane **78**, 045426 (2008)*

b)

c)

Band evolution of Bi$_{1-x}$Sb$_x$ using tight-binding method

FIG. 19 (a) Rhombohedral structure of Bi-based materials and layers showing a 6 atomic plane stacking in the unit cell along the normal (111) crystallographic direction. Parametrization used in Ref. Teo *et al.* (2008) for Bi$_{1-x}$Sb$_x$ alloys with the typical wrapping term. (b) Evidence of the two surface states (Σ_1 and Σ_2) obtained with a semi-infinite Bi$_{0.79}$Sb$_{0.21}$ with $x = 0.21$. (c) Band evolution of Bi$_{1-x}$Sb$_x$ using the tight-binding method and geometrical domain in the x-space (Sb content) displaying the topological surface states.

per unit cell, forming a bilayer (BL) structure. The lattice parameters were chosen to be the ones of the bulk corresponding to $a = 4.7235$ Å and $\alpha_{rho} = 57.35^o$ as detailed in the paper of Liu and Allen (1995). Bi thin film is obtained by stacking the BLs along the (111) direction, such as the z axis. The surface is thus parallel to the xy plane. The uppermost and lowermost BLs are in contact with a vacuum. We first construct a model Hamiltonian for the Bi thin film. For this purpose, the sp_3 TB model, we chose for the bulk Bi crystal (results not shown) is adapted to the Bi thin film. There are s, p_x, p_y, and p_z orbitals with spin index σ on each atom. The hopping terms among the atomic orbitals are decomposed into respective inter- and intra-BL hopping terms. The inter-BL hopping term $H_{21} - 2$ consists of the nearest-neighbor hopping term in the bulk Bi Hamiltonian, whereas the intra-BL hopping term consists of two parts, H_{11} and $H_{12} - 1$, with the third and second nearest neighbor hopping terms in the bulk model, respectively (Ohtsubo and Kimura, 2016; Saito *et al.*, 2016). There is a surface potential gradient on the surface BL along the z axis between the surface Bi atoms and the vacuum. The surface Rashba effect is induced by the contribution of this potential gradient. In terms of the sp_3 TB model, this is described by the following spin independent hopping terms between the nearest-neighbor sites. In order to take into account top and bottom surface Rashba states,

we introduced supplementary hopping terms of adequate symmetry taking into account the asymmetric potential terms due to the symmetry breaking, and as developed in several situations (Saito *et al.*, 2016).

The Bi and Sb in A7 crystal structures, as well as Bi$_{1-x}$Sb$_x$ alloys with $x = 0.2, 0.3, 0.4$ were then calculated using the tight-binding methods and different possible parametrizations like given by either Liu and Allen (1995), Teo *et al.* (2008), or Ohtsubo and Kimura (2016). Two surface sates, namely Σ_1 and Σ_2 were found in the gap. A transition from Trivial to non-trivial topological surface states were found depending on the number of band crossings with the Fermi levels in the Bi host gap, and the spin-texture of those surface states has been extracted.

B. Co/Fe overlayers on Bi

As perspective for future work, we have to:

- evaluate the behavior of the spin-texture surface states of BiSb with top ferromagnetic Co overlayer able to produce the spin-current.

- Calculate the *intrinsic* and *extrinsic* spin and charge conductivity by differentiating respective *bulk* and *surface* contributions.

- Calculations of the optical spectra of bulk Bi, Sb, and BiSb for comparison to measurements are currently being carried out by partner VSB. A summary of the performed calculations and comparison with experiments is provided in the Technical Report for the first reporting period.

V. OUTLOOK

The *ab initio* calculations and modeling performed for the deliverable D3.1 have brought a number of interesting findings to the light, which are relevant for measurements performed within the consortium. Beyond the current workplan of the project, drafted two years ago, there are new developments that can have significance for future developments in what is now becoming called "orbitronics".

The theoretical studies performed suggest a number of experimental investigations that could be carried out in the consortium:

- Measure the predicted spin accumulations due to the SREE and SHE separately for the bilayer systems Pt/Co and Pt/Ni, if possible in a layer-resolved way.

- Measure the *ab initio* predicted orbital polarization in the bi-metallic layers.

- Confirm the existence of the new predicted M-longitudinal component (having both spin and orbital components). The spin/orbital polarization induced in this component does not contribute to the SOT, but an observation of its existence would imply a major confirmation of the employed theoretical framework.

- The current-induced spin and orbital polarizations due to the SREE and OREE have been predicted for Mn_2Au and CuMnAs; dedicated measurements of these polarizations are required to compare with the theoretical values.

- The theory predicts SOTs in the AFMs Mn_2Au and CuMnAs at petahertz (PHz) frequencies. This is to be tested in measurements.

- The dependences of the spin and orbital polarization due to SHE/SREE and OHE/OREE on the magnetization direction has been computed. It would be worthwhile to confirm the magnetization direction dependence in experiments.

- For a full comparison with experiments, it will be needed to compute also the SHE and OHE of CuMnAs and Mn_2Au. In addition, it would be worthwhile to perform calculations for bilayer structures, such as Pt/CuMnAs and Pt/Mn_2Au. Such calculations could shed light on THz emission from these bilayer systems.

- Once the structural optimization of Fe/Bi and Co/Bi (or Fe/BiSb, Co/BiSb) bilayers has been done, it will be worthwhile to compute the induced spin and orbital polarizations in these bilayer systems, to understand the process of spin-to-charge conversion and how it could be possibly enhanced.

REFERENCES

Amin, V. P., and M. D. Stiles (2016), Phys. Rev. B **94**, 104420.

Amin, V. P., J. Zemen, and M. D. Stiles (2018), Phys. Rev. Lett. **121** (13), 136805.

Baltz, V., A. Manchon, M. Tsoi, T. Moriyama, T. Ono, and Y. Tserkovnyak (2018), Rev. Mod. Phys. **90**, 015005.

von Barth, U., and L. Hedin (1972), J. Phys. C: Solid State Phys. **5** (13), 1629.

Barthem, V. M. T. S., C. V. Colin, H. Mayaffre, M. H. Julien, and D. Givord (2013), Nat. Commun. **4**, 2892.

Battiato, M., K. Carva, and P. M. Oppeneer (2010), Phys. Rev. Lett. **105**, 027203.

Battiato, M., K. Carva, and P. M. Oppeneer (2012), Phys. Rev. B **86** (2), 024404.

Baumgartner, M., K. Garello, J. Mendil, C. O. Avci, E. Grimaldi, C. Murer, J. Feng, M. Gabureac, C. Stamm, Y. Acremann, S. Finizio, S. Wintz, J. Raabe, and P. Gambardella (2017), Nat. Nanotechn. **12** (10), 980.

Belashchenko, K. D., A. A. Kovalev, and M. van Schilfgaarde (2019), Phys. Rev. Materials **3**, 011401.

Benia, H. M., C. Straßer, K. Kern, and C. R. Ast (2015), Phys. Rev. B **91**, 161406.

Berger, A. J., E. R. J. Edwards, H. T. Nembach, A. D. Karenowska, M. Weiler, and T. J. Silva (2018), Phys. Rev. B **97**, 094407.

Blaha, P., K. Schwarz, G. K. H. Madsen, D. Kvasnicka, J. Luitz, R. Laskowski, F. Tran, and L. D. Marks (2018), *WIEN2k, An Augmented Plane Wave + Local Orbitals Program for Calculating Crystal Properties (Karlheinz Schwarz, Techn. Universität Wien, Austria)*.

Bodnar, S. Y., L. Šmejkal, I. Turek, T. Jungwirth, O. Gomonay, J. Sinova, A. A. Sapozhnik, H.-J. Elmers, M. Kläui, and M. Jourdan (2018), Nat. Commun. **9** (1), 348.

Boiko, I. I., and E. I. Rashba (1960), Sov. Phys. Solid State **2**, 1692.

Brataas, A., A. D. Kent, and H. Ohno (2012), Nat. Mater. **11** (5), 372.

Bychkov, Y. A., and E. I. Rashba (1984), JETP Lett. **39**, 78.

Carva, K., M. Battiato, D. Legut, and P. M. Oppeneer (2013), Phys. Rev. B **87**, 184425.

Chen, X., Y. Liu, G. Yang, H. Shi, C. Hu, M. Li, and H. Zeng (2018), Nat. Commun. **9**, 2569.

Chi, Z., Y.-C. Lau, X. Xu, T. Ohkubo, K. Hono, and M. Hayashi (2020), Sci. Adv. **6** (10), eaay2324.

Ciccarelli, C., L. Anderson, V. Tshitoyan, A. J. Ferguson, F. Gerhard, C. Gould, L. W. Molenkamp, J. Gayles, J. Železný, L. Šmejkal, Z. Yuan, J. Sinova, F. Freimuth, and T. Jungwirth (2016), Nat. Phys. **12** (9), 855.

Dang, T. H., Q. Barbedienne, D. Q. To, E. Rongione, N. Reyren, F. Godel, S. Collin, J. M. George, and H. Jaffrès (2020), Phys. Rev. B **102**, 144405.

Ding, S., A. Ross, D. Go, L. Baldrati, Z. Ren, F. Freimuth, S. Becker, F. Kammerbauer, J. Yang, G. Jakob, Y. Mokrousov, and M. Kläui (2020), Phys. Rev. Lett. **125**, 177201.

Dolui, K., and B. K. Nikolić (2017), Phys. Rev. B **96**, 220403.

Du, Y., H. Gamou, S. Takahashi, S. Karube, M. Kohda, and J. Nitta (2020), Phys. Rev. Applied **13**, 054014.

D'yakonov, M. I., and V. I. Perel' (1971), JETP Lett **13**, 467.

Edelstein, V. M. (1990), Solid State Commun. **73** (3), 233.

Eschenlohr, A., M. Battiato, P. Maldonado, N. Pontius, T. Kachel, K. Holldack, R. Mitzner, A. Föhlisch, P. M. Oppeneer, and C. Stamm (2013), Nature Mater. **12**, 332.

Evans, R. F. L., W. J. Fan, P. Chureemart, T. A. Ostler, M. O. A. Ellis, and R. W. Chantrell (2014), J. Phys.: Condens. Matter **26** (10), 103202.

Fan, X., H. Celik, J. Wu, C. Ni, K.-J. Lee, V. O. Lorenz, and J. Q. Xiao (2014), Nat. Commun. **5**, 3042.

Fan, X., J. Wu, Y. Chen, M. J. Jerry, H. Zhang, and J. Q. Xiao (2013), Nat. Commun. **4**, 1799.

Fiebig, M., N. P. Duong, T. Satoh, B. B. Van Aken, K. Miyano, Y. Tomioka, and Y. Tokura (2008), J. Phys. D: Appl. Phys. **41** (16), 164005.

Freeman, R., A. Zholud, Z. Dun, H. Zhou, and S. Urazhdin (2018), Phys. Rev. Lett. **120**, 067204.

Freimuth, F., S. Blügel, and Y. Mokrousov (2014), Phys. Rev. B **90**, 174423.

Freimuth, F., S. Blügel, and Y. Mokrousov (2015), Phys. Rev. B **92**, 064415.

Garello, K., C. O. Avci, M. I. Miron, M. Baumgartner, A. Ghosh, S. Auffret, O. Boulle, G. Gaudin, and P. Gambardella (2013), Appl. Phys. Lett. **105** (21), 212402.

Ghosh, A., S. Auffret, U. Ebels, and W. E. Bailey (2012), Phys. Rev. Lett. **109**, 127202.

Go, D., F. Freimuth, J.-P. Hanke, F. Xue, O. Gomonay, K.-J. Lee, S. Blügel, P. M. Haney, H.-W. Lee, and Y. Mokrousov (2020), Phys. Rev. Research **2**, 033401.

Go, D., J.-P. Hanke, P. M. Buhl, F. Freimuth, G. Bihlmayer, H.-W. Lee, Y. Mokrousov, and S. Blügel (2017), Sci. Rep. **7**, 46742.

Go, D., D. Jo, C. Kim, and H.-W. Lee (2018), Phys. Rev. Lett. **121** (8), 086602.

Go, D., and H.-W. Lee (2020), Phys. Rev. Research **2**, 013177.

Godinho, J., H. Reichlová, D. Kriegner, V. Novák, K. Olejník, Z. Kašpar, Z. Šobáň, P. Wadley, R. P. Campion, R. M. Otxoa, P. E. Roy, J. Železný, T. Jungwirth, and J. Wunderlich (2018), Nat. Commun. **9**, 4686.

Grzybowski, M. J., P. Wadley, K. W. Edmonds, R. Beardsley, V. Hills, R. P. Campion, B. L. Gallagher, J. S. Chauhan, V. Novak, T. Jungwirth, F. Maccherozzi, and S. S. Dhesi (2017), Phys. Rev. Lett. **118** (5), 057701.

Gunnarsson, O., O. Jepsen, and O. K. Andersen (1983), Phys. Rev. B **27**, 7144.

Guo, G. Y., S. Murakami, T.-W. Chen, and N. Nagaosa (2008), Phys. Rev. Lett. **100** (9), 096401.

Guo, G. Y., Y. Yao, and Q. Niu (2005), Phys. Rev. Lett. **94**, 226601.

Hanke, J.-P., F. Freimuth, S. Blügel, and Y. Mokrousov (2017), Sci. Rep. **7**, 41078.

Hellman, F., A. Hoffmann, Y. Tserkovnyak, G. S. D. Beach, E. E. Fullerton, C. Leighton, A. H. MacDonald, D. C. Ralph, D. A. Arena, H. A. Dürr, P. Fischer, J. Grollier, J. P. Heremans, T. Jungwirth, A. V. Kimel, B. Koopmans, I. N. Krivorotov, S. J. May, A. K. Petford-Long, J. M. Rondinelli, N. Samarth, I. K. Schuller, A. N. Slavin, M. D. Stiles, O. Tchernyshyov, A. Thiaville, and B. L. Zink (2017), Rev. Mod. Phys. **89**, 025006.

Hirsch, J. E. (1999), Phys. Rev. Lett. **83** (9), 1834.

Hoffmann, A. (2013), IEEE Trans. Magn. **49**, 5172.

Hofherr, M., P. Maldonado, O. Schmitt, M. Berritta, U. Bierbrauer, S. Sadashivaiah, A. J. Schellekens, B. Koopmans, D. Steil, M. Cinchetti, B. Stadtmüller, P. M. Oppeneer, S. Mathias, and M. Aeschlimann (2017), Phys. Rev. B **96**, 100403.

Hsieh, D., D. Qian, L. Wrey, Y. Xia, Y. S. Hor, R. J. Cava, and M. Z. Hasan (2008), Nature **452**, 970.

Ishida, H. (2016), J. Phys.: Condens. Matter **29** (1), 015002.

Jo, D., D. Go, and H.-W. Lee (2018), Phys. Rev. B **98**, 214405.

Johansson, A., J. Henk, and I. Mertig (2018), Phys. Rev. B **97**, 085417.

Jungfleisch, M. B., Q. Zhang, W. Zhang, J. E. Pearson, R. D. Schaller, H. Wen, and A. Hoffmann (2018), Phys. Rev. Lett. **120**, 207207.

Jungfleisch, M. B., W. Zhang, R. Winkler, and A. Hoffmann (2017), in *Spin Physics in Semiconductors*, Vol. 157, edited by M. Dyakonov (Springer, Berlin) pp. 355–385.

Jungwirth, T., X. Marti, P. Wadley, and J. Wunderlich (2016), Nat. Nanotechn. **11**, 231.

Kampfrath, T., M. Battiato, P. Maldonado, G. Eilers, J. Notzold, S. Mahrlein, V. Zbarsky, F. Freimuth, Y. Mokrousov, S. Blügel, M. Wolf, I. Radu, P. M. Oppeneer, and M. Münzenberg (2013), Nature Nanotechn. **8**, 256.

Kampfrath, T., A. Sell, G. Klatt, A. Pashkin, S. Mährlein, T. Dekorsy, M. Wolf, M. Fiebig, A. Leitenstorfer, and R. Huber (2010), Nat. Photon. **5** (1), 31.

Kato, Y. K., R. C. Myers, A. C. Gossard, and D. D. Awschalom (2004a), Phys. Rev. Lett. **93** (17), 176601.

Kato, Y. K., R. C. Myers, A. C. Gossard, and D. D. Awschalom (2004b), Science **306** (5703), 1910.

Kim, J., D. Go, H. Tsai, D. Jo, K. Kondou, H.-W. Lee, and Y. Otani (2020), "Non-trivial charge-to-spin conversion in ferromagnetic metal/Cu/Al$_2$O$_3$ by orbital transport," arXiv:2002.00596 [cond-mat.mes-hall].

Kim, J., J. Sinha, M. Hayashi, M. Yamanouchi, S. Fukami, T. Suzuki, S. Mitani, and H. Ohno (2013), Nat. Mater. **12** (3), 240.

Kim, T. H., P. Grünberg, S. H. Han, and B. K. Cho (2017), Sci. Rep. **7**, 4515.

Kimel, A. V., B. A. Ivanov, R. V. Pisarev, P. A. Usachev, A. Kirilyuk, and T. Rasing (2009), Nat. Phys. **5** (10), 727.

Kimel, A. V., A. Kirilyuk, A. Tsvetkov, R. V. Pisarev, and T. Rasing (2004), Nature **429** (6994), 850.

Kirilyuk, A., A. V. Kimel, and T. Rasing (2010), Rev. Mod. Phys. **82**, 2731.

Kittel, C. (1946), Phys. Rev. **70**, 281.

Kontani, H., T. Tanaka, D. S. Hirashima, K. Yamada, and J. Inoue (2009), Phys. Rev. Lett. **102**, 016601.

Koroteev, Y. M., G. Bihlmayer, E. V. Chulkov, and S. Blügel (2008), Phys. Rev. B **77**, 045428.

Kurebayashi, H., J. Sinova, D. Fang, A. C. Irvine, T. D. Skinner, J. Wunderlich, V. Novák, R. P. Campion, B. L. Gallagher, E. K. Vehstedt, L. P. Zârbo, K. Výborný, A. J. Ferguson, and T. Jungwirth (2014), Nat. Nanotechn. **9** (3),

211.

Kurt, H., R. Loloee, K. Eid, W. P. Pratt, and J. Bass (2003), Appl. Phys. Lett. **81** (25), 4787.

Levitov, L. S., Y. V. Nazarov, and G. M. Éliashberg (1985), Sov. Phys. JETP. **61**, 133.

Li, D., S. Chen, Y. Zuo, J. Yun, B. Cui, K. Wu, X. Guo, D. Yang, J. Wang, and L. Xi (2018), Sci. Rep. **8**, 12959.

Liu, L., T. Moriyama, D. C. Ralph, and R. A. Buhrman (2011), Phys. Rev. Lett. **106** (3), 036601.

Liu, L., C. F. Pai, Y. Li, H. W. Tseng, D. C. Ralph, and R. A. Buhrman (2012), Science **336** (6081), 555.

Liu, Y., and R. E. Allen (1995), Phys. Rev. B **52**, 1566.

Lu, W.-T., Y. Zhao, M. Battiato, Y. Wu, and Z. Yuan (2020), Phys. Rev. B **101**, 014435.

Máca, F., J. Mašek, O. Stelmakhovych, X. Martí, H. Reichlová, K. Uhlířová, P. Beran, P. Wadley, V. Novák, and T. Jungwirth (2012), J. Magn. Magn. Mater. **324** (8), 1606.

Mahfouzi, F., and N. Kioussis (2018), Phys. Rev. B **97**, 224426.

Mahfouzi, F., R. Mishra, P.-H. Chang, H. Yang, and N. Kioussis (2020), Phys. Rev. B **101**, 060405.

Maldonado, P., K. Carva, M. Flammer, and P. M. Oppeneer (2017), Phys. Rev. B **96**, 174439.

Malinowski, G., N. Bergeard, M. Hehn, and S. Mangin (2018), Eur. Phys. J. B **91**, 98.

Manchon, A., and A. Belabbes (2017), Solid State Phys. **68**, 1.

Manchon, A., H. C. Koo, J. Nitta, S. M. Frolov, and R. A. Duine (2015), Nat. Mater. **14** (9), 871.

Manchon, A., J. Železný, I. M. Miron, T. Jungwirth, J. Sinova, A. Thiaville, K. Garello, and P. Gambardella (2019), Rev. Mod. Phys. **91**, 035004.

Meinert, M., D. Graulich, and T. Matalla-Wagner (2018), Phys. Rev. Applied **9**, 064040.

Miron, M. I., K. Garello, G. Gaudin, P. J. Zermatten, M. V. Costache, S. Auffret, S. Bandiera, B. Rodmacq, A. Schuhl, and P. Gambardella (2011), Nature **476** (7359), 189.

Miron, M. I., G. Gaudin, S. Auffret, B. Rodmacq, A. Schuhl, S. Pizzini, J. Vogel, and P. Gambardella (2010), Nat. Mater. **9** (3), 230.

Mondal, R., M. Berritta, A. K. Nandy, and P. M. Oppeneer (2017), Phys. Rev. B **96**, 024425.

Němec, P., M. Fiebig, T. Kampfrath, and A. V. Kimel (2018), Nat. Phys. **14**, 229.

Nenno, D. M., B. Rethfeld, and H. C. Schneider (2018), Phys. Rev. B **98**, 224416.

Nguyen, H. Y. T., W. P. Pratt, and J. Bass (2014), J. Magn. Magn. Mater. **361**, 30.

Nowak, U. (2007), in *Handbook of Magnetism and Advanced Magnetic Materials*, Vol. 2, edited by H. Kronmüller and S. Parkin (J. Wiley Sons, Chichester).

Ohtsubo, Y., and S.-i. Kimura (2016), New J. Phys. **18** (12), 123015.

Olejník, K., V. Schuler, X. Marti, V. Novák, Z. Kašpar, P. Wadley, R. P. Campion, K. W. Edmonds, B. L. Gallagher, J. Garces, M. Baumgartner, P. Gambardella, and T. Jungwirth (2017), Nat. Commun. **8**, 15434.

Olejník, K., T. Seifert, Z. Kašpar, V. Novák, P. Wadley, R. P. Campion, M. Baumgartner, P. Gambardella, P. Němec, J. Wunderlich, J. Sinova, P. Kužel, M. Müller, T. Kampfrath, and T. Jungwirth (2018), Sci. Adv. **4**, eaar3566.

Pashkin, A., A. Sell, T. Kampfrath, and R. Huber (2013),

New J. Phys. **15** (6), 065003.

Pashov, D., S. Acharya, W. R. L. Lambrecht, J. Jackson, K. D. Belashchenko, A. Chantis, F. Jamet, and M. van Schilfgaarde (2019), arXiv:1907.06021.

Ritzmann, U., P. Baláž, P. Maldonado, K. Carva, and P. M. Oppeneer (2020), Phys. Rev. B **101**, 174427.

Rojas-Sánchez, J. C., N. Reyren, P. Laczkowski, W. Savero, J. P. Attané, C. Deranlot, M. Jamet, J. M. George, L. Vila, and H. Jaffrès (2014), Phys. Rev. Lett. **112** (10), 106602.

Rudolf, D., C. La-O-Vorakiat, M. Battiato, R. Adam, J. M. Shaw, E. Turgut, P. Maldonado, S. Mathias, P. Grychtol, H. T. Nembach, T. J. Silva, M. Aeschlimann, H. C. Kapteyn, M. M. Murnane, C. M. Schneider, and P. M. Oppeneer (2012), Nature Commun. **3**, 1037.

Safeer, C. K., E. Jué, A. Lopez, L. Buda-Prejbeanu, S. Auffret, S. Pizzini, O. Boulle, I. M. Miron, and G. Gaudin (2016), Nat. Nanotechn. **11**, 143.

Saito, K., H. Sawahata, T. Komine, and T. Aono (2016), Phys. Rev. B **93**, 041301.

Salemi, L., M. Berritta, A. K. Nandy, and P. M. Oppeneer (2019), Nat. Commun. **10** (1), 538.

Schep, K. M., J. van Hoof, P. J. Kelly, G. E. W. Bauer, and J. E. Inglesfield (1997), Phys. Rev. B **56**, 10805.

Sinova, J., S. O. Valenzuela, J. Wunderlich, C. H. Back, and T. Jungwirth (2015), Rev. Mod. Phys. **87** (4), 1213.

Soler, J. M., E. Artacho, J. D. Gale, A. García, J. Junquera, P. Ordejón, and D. Sánchez-Portal (2002), J. Phys.: Condens. Matter **14** (11), 2745.

Stamm, C., C. Murer, Y. Acremann, M. Baumgartner, R. Gort, S. Däster, A. Kleibert, K. Garello, J. Feng, M. Gabureac, Z. Chen, J. Stöhr, and P. Gambardella (2019), Phys. Rev. B **100**, 024426.

Stamm, C., C. Murer, M. Berritta, J. Feng, M. Gabureac, P. M. Oppeneer, and P. Gambardella (2017), Phys. Rev. Lett. **119** (8), 087203.

Tanaka, T., H. Kontani, M. Naito, T. Naito, D. S. Hirashima, K. Yamada, and J. Inoue (2008), Phys. Rev. B **77**, 165117.

Tao, X., Q. Liu, B. Miao, R. Yu, Z. Feng, L. Sun, B. You, J. Du, K. Chen, S. Zhang, L. Zhang, Z. Yuan, D. Wu, and H. Ding (2018), Sci. Adv. **4** (6), aat1670.

Tazaki, Y., Y. Kageyama, H. Hayashi, T. Harumoto, T. Gao, J. Shi, and K. Ando (2020), "Current-induced torque originating from orbital current," arXiv:2004.09165 [cond-mat.mtrl-sci].

Teo, J. C. Y., L. Fu, and C. L. Kane (2008), Phys. Rev. B **78**, 045426.

Tokatly, I. V., E. E. Krasovskii, and G. Vignale (2015), Phys. Rev. B **91**, 035403.

Turek, I., V. Drchal, J. Kudrnovsky, M. Sob, and P. Weinberger (1997), *Electronic Structure of Disordered Alloys, Surfaces and Interfaces* (Springer, New York).

Valet, T., and A. Fert (1993), Phys. Rev. B **48**, 7099.

Baláž, P., K. Carva, U. Ritzmann, P. Maldonado, and P. M. Oppeneer (2020), Phys. Rev. B **101**, 174418.

Wadley, P., V. Hills, M. R. Shahedkhah, K. W. Edmonds, R. P. Campion, V. Novák, B. Ouladdiaf, D. Khalyavin, S. Langridge, V. Saidl, P. Němec, A. W. Rushforth, B. L. Gallagher, S. S. Dhesi, F. Maccherozzi, J. Železný, and T. Jungwirth (2015), Sci. Rep. **5**, 17079.

Wadley, P., B. Howells, J. Železný, C. Andrews, V. Hills, R. P. Campion, V. Novák, F. Freimuth, Y. Mokrousov, A. W. Rushforth, K. W. Edmonds, B. L. Gallagher, and T. Jungwirth (2016), Science **351** (6273), 587.

Wadley, P., V. Novák, R. P. Campion, C. Rinaldi, X. Martí,

H. Reichlová, J. Železný, J. Gazquez, M. A. Roldan, M. Varela, D. Khalyavin, S. Langridge, D. Kriegner, F. Máca, J. Mašek, R. Bertacco, V. Holý, A. W. Rushforth, K. W. Edmonds, B. L. Gallagher, C. T. Foxon, J. Wunderlich, and T. Jungwirth (2013), Nat. Commun. **4**, 2322.

Wadley, P., S. Reimers, M. J. Grzybowski, C. Andrews, M. Wang, J. S. Chauhan, B. L. Gallagher, R. P. Campion, K. W. Edmonds, S. S. Dhesi, F. Maccherozzi, V. Novák, J. Wunderlich, and T. Jungwirth (2018), Nat. Nanotechn. **13**, 362.

Wang, L., R. J. H. Wesselink, Y. Liu, Z. Yuan, K. Xia, and P. J. Kelly (2016), Phys. Rev. Lett. **116**, 196602.

Wimmer, S., K. Chadova, M. Seemann, D. Ködderitzsch, and H. Ebert (2016), Phys. Rev. B **94**, 054415.

Wunderlich, J., B. Kaestner, J. Sinova, and T. Jungwirth (2005), Phys. Rev. Lett. **94** (4), 047204.

Xiao, J., Y. Liu, and B. Yan (2020), "Detection of the Orbital Hall Effect by the Orbital-Spin Conversion," arXiv:2010.01970 [cond-mat.mtrl-sci].

Yamaoka, T. (1974), J. Phys. Soc. Jpn. **36** (2), 445.

Yoda, T., T. Yokoyama, and S. Murakami (2018), Nano Lett. **18**, 916.

Železný, J., H. Gao, A. Manchon, F. Freimuth, Y. Mokrousov, J. Zemen, J. Mašek, J. Sinova, and T. Jungwirth (2017), Phys. Rev. B **95** (1), 14403.

Železný, J., H. Gao, K. Výborný, J. Zemen, J. Mašek, A. Manchon, J. Wunderlich, J. Sinova, and T. Jungwirth (2014), Phys. Rev. Lett. **113** (15), 157201.

Zhang, S. (2000), Phys. Rev. Lett. **85** (2), 393.

Zhou, C., Y. P. Liu, Z. Wang, S. J. Ma, M. W. Jia, R. Q. Wu, L. Zhou, W. Zhang, M. K. Liu, Y. Z. Wu, and J. Qi (2018), Phys. Rev. Lett. **121**, 086801.

Zhu, L., and R. A. Buhrman (2020), "Absence of spin current generation in Ti/FeCoB bilayers with strong interfacial spin-orbit coupling," arXiv:2010.13137 [cond-mat.mes-hall].

Zhukov, V. P., E. V. Chulkov, and P. M. Echenique (2005), Phys. Rev. B **72** (15), 155109.

Zhukov, V. P., E. V. Chulkov, and P. M. Echenique (2006), Phys. Rev. B **73** (12), 125105.

Žutić, I., J. Fabian, and S. Das Sarma (2004), Rev. Mod. Phys. **76** (2), 323.